

# Intelligent Attractors for Singularly Perturbed Dynamical Systems\*

Daniel A. Serino<sup>†</sup>, Allen Alvarez Loya<sup>†</sup>, J. W. Burby<sup>‡</sup>, Ioannis G. Kevrekidis<sup>§</sup>, and Qi Tang<sup>†</sup>

**Abstract.** Singularly perturbed dynamical systems, commonly known as fast-slow systems, play a crucial role in various applications such as plasma physics. They are closely related to reduced order modeling, closures, and structure-preserving numerical algorithms for multiscale modeling. A powerful and well-known tool to address these systems is the Fenichel normal form, which significantly simplifies fast dynamics near slow manifolds through a transformation. However, the Fenichel normal form is difficult to realize in conventional numerical algorithms. In this work, we explore an alternative way of realizing it through structure-preserving machine learning. Specifically, a fast-slow neural network (FSNN) is proposed for learning data-driven models of singularly perturbed dynamical systems with dissipative fast timescale dynamics. Our method enforces the existence of a trainable, attracting invariant slow manifold as a hard constraint. Closed-form representation of the slow manifold enables efficient integration on the slow time scale and significantly improves prediction accuracy beyond the training data. We demonstrate the FSNN on several examples that exhibit multiple timescales, including the Grad moment system from hydrodynamics, two-scale Lorentz96 equations for modeling atmospheric dynamics, and Abraham-Lorentz dynamics modeling radiation reaction of electrons in a magnetic field.

**Key words.** Singularly perturbed dynamical systems, slow manifold, model discovery, closures

**1. Introduction.** In this article, a new architecture called the Fast-Slow Neural Network (FSNN) is developed for learning data-driven models of fast-slow dynamical systems with dissipative fast timescale dynamics. Our method enforces the existence of a trainable, attracting invariant slow manifold [10] as a hard constraint. The constraint is imposed by way of a novel neural network architecture with structured weight matrices. By leveraging the neural ODE framework from [11], our technique produces deterministic evolution equations that approximately reproduce trajectory training data. When the training data comes from an unknown dynamical system, the method achieves data-driven *full-order* model discovery with stability guarantees due to provable existence of the slow manifold. In short, our architecture strongly contains an attractor of singularly perturbed dynamical systems by design.

Various dynamical systems encountered in nature exhibit a timescale separation such that the fast timescale is dissipative. Prominent examples include the kinetic dynamics of strongly-collisional gasses and plasmas, and radiative transfer in optically-thick media. For ordinary differential equations (ODEs) of this type, Fenichel theory [21] reveals that fast timescale dissipation implies existence of an invariant slow manifold that attracts nearby trajectories

\*Submitted to the editors February 2024. Corresponding author: [qtang@lanl.gov](mailto:qtang@lanl.gov)

**Funding:** This work was partially supported by the U.S. Department of Energy Advanced Scientific Computing Research (ASCR) under DOE-FOA-2493 “Data-intensive scientific machine learning”. It was also partially supported by the ASCR program of Mathematical Multifaceted Integrated Capability Center (MMICC). Alvarez Loya is supported by the U.S. National Science Foundation under NSF-DMS-2213261.

<sup>†</sup>Los Alamos National Laboratory, Los Alamos, NM ([dserino@lanl.gov](mailto:dserino@lanl.gov), [aalvarezloya@lanl.gov](mailto:aalvarezloya@lanl.gov), [qtang@lanl.gov](mailto:qtang@lanl.gov)).

<sup>‡</sup>Department of Physics, University of Texas at Austin, Austin, TX ([joshua.burby@austin.utexas.edu](mailto:joshua.burby@austin.utexas.edu))

<sup>§</sup>Department of Chemical and Biomolecular Engineering and Department of Applied Mathematics and Statistics, Johns Hopkins University, Baltimore, MD ([yannisk@jhu.edu](mailto:yannisk@jhu.edu)).

and governs the long-term dynamics. For partial differential equations (PDEs), or more generally integro-differential equations, Fenichel theory generally only applies formally, but its predictions are often valid anyway. For PDEs, inertial manifold theory [24] has been studied and shown to be useful in applications such as model reductions of fluid dynamics.

Nonlinear dimensionality reduction inspired by inertial manifold theory has a rich history (see [36] and the references therein) originating in the 1980s and 1990s [22, 24, 23, 33, 56, 57, 31, 28]. Data-driven approaches for discovering inertial manifolds in dynamical systems and using separations of scales to evolve a lower-dimensional reduced order model first materialized in the 90s [34, 59, 37, 38, 55, 53, 54] and recently reemerged in popularity due to boom in machine-learning-based modeling [4, 12, 48, 3, 39, 42, 61, 43, 60, 16, 44, 41]. The work in this manuscript tackles a special class of systems with attracting invariant sets, namely fast-slow systems with dissipative fast timescale dynamics [10]. Unlike previous data-driven approaches, the FSNN is a *full-order* model which, through the use of neural network architectures with special properties, strictly enforces the existence of an attracting slow manifold. This method may be viewed as a major step along a pathway in developing data-driven model discovery techniques with embedded invariant manifolds that do not use explicit timescale separation as a crutch.

The secondary goal of the proposed network is to discover an efficient and asymptotic-preserving *reduced-order* model. In the common methodology of physics-based model reduction, one first decides a latent space (e.g. lower-order moments of a distribution) and then looks for a closure using tools such as asymptotic analysis. Many complicated closures have been discovered through this approach. The classical examples in rarefied gases and plasma physics include Grad’s moment method [27], Braginskii closure [8] and Hammett-Perkins closure [29]. The challenge of this methodology is that an exact closure may not exist. The accuracy of the approximate closure is related to the dimension of the latent space. In contrast, Fenichel theory guarantees the existence of an exact closure in the neighborhood of the singular limit of the equations in the form of a diffeomorphic coordinate transformation. This transformation exposes an invariant manifold by flattening the fast variable space. Often in practice, as asymptotic expansion is the best analytical approximation to the exact closure. In our work, we leverage structured neural network architectures and optimization to learn an approximation to the exact closure that is hidden in the dynamics. The data-driven approach described in this work can discover such a transformation only using short-term trajectory data. Therefore, this approach may be useful when the underlying dynamical system is known but the targeting latent space or a formal closure are not known.

The design of the FSNN architecture is motivated by the the first few theorems discovered by Fenichel [35]. The components of the architecture are constructed using structured weight matrices. The coordinate transformation into Fenichel normal form is based on an invertible coupling flow network [58] in which we introduced the additional structure-preserving property of bi-Lipschitz control through the use of bi-Lipschitz affine transformation (bLAT) layers. This network and its inverse can be evaluated using closed-form expressions with identical computational complexity. We note that “vanilla” neural networks are generally non-invertible [25, 52, 14]. We also introduce the Schur form network, which is a novel architecture based on the Schur decomposition for controlling the locations of eigenvalues in the complex plane, to parameterize the linear term in the dynamics. Additionally, a low-rank

bilinear form network is included to increase the approximation power in the fast variable space. Our approach is then integrated using adaptive time stepping that treats the linear term implicitly, further leveraging back-substitution on the Schur form. Some of the structures introduced are related to the idea of trivializing manifold optimization through parameterizations [40]. Structure-preserving flow maps through machine learning are an active area of research, and include such as the symplectic neural networks for Hamiltonian dynamics [32, 9]. Previous studies on flow map learning for multi-scale dynamical systems include [46] and [20]. In particular, [20] simultaneously preserves symplecticity and adiabatic invariance in a multi-scale setting.

Before going into a detailed presentation of our new method, it is worth highlighting an important shortcoming it suffers from, and how that shortcoming might be mitigated in practice. The method assumes that the dimension of the attracting invariant manifold is known in advance. While this is not a limitation in the surrogate modeling context, where the (expensive to simulate) dynamical system is known in detail, it does present a moderate challenge in the model discovery context. As such, when performing data-driven model discovery using our method, it will be necessary to first determine the dimension of the slow manifold, either through physical reasoning, or through application of auxiliary data mining techniques such as diffusion maps [13], autoencoders [61], or other techniques from reduced order modeling [36].

The remainder of the manuscript is organized as follows. A review of fast-slow dynamical systems is presented in Section 2. The fast-slow neural network architecture is described in detail in Section 3. The numerical implementation of the architecture is presented in Section 4. Results from applying the architecture to various examples are shown in Section 5. Concluding remarks are made in Section 6.

**2. Fast-Slow Dynamics and the Fenichel Normal Form.** In this paper, we develop a novel machine learning (ML)-inspired architecture, the Fast-Slow Neural Network (FSNN). FSNNs are a parameterization for a class of dynamical systems exhibiting multiscale behavior in time that, to leading order, are dissipative on the fast time scale. Fast-slow systems, which exhibit both short-term and long-term behavior, are relevant to many physical systems observed in nature, including the climate and plasma systems. In this section, we motivate the FSNN architecture with a review the theory of fast-slow systems.

**Definition 2.1.** *A fast-slow system is an ODE of the form [10]*

$$(2.1a) \quad \epsilon \frac{d}{d\tau} y = f(x, y, \epsilon),$$

$$(2.1b) \quad \frac{d}{d\tau} x = g(x, y, \epsilon),$$

where  $x = x(\tau) \in \mathbb{R}^{N_x}$ ,  $y = y(\tau) \in \mathbb{R}^{N_y}$ ,  $f$  and  $g$  are smooth functions of their arguments, and  $D_y f(x, y, 0)$  is invertible for all  $(x, y)$  where  $f(x, y, 0) = 0$ .

In the above definition,  $y$  and  $x$  are the fast and slow variables, respectively, over corresponding timescale variables  $t$  and  $\tau = \epsilon t$ .

In some instances, a dynamical system may exhibit a fast-slow split, but a representation for the fast and slow variables is unknown. Consider the following representation of a

dynamical system for  $z(\tau) \in \mathbb{R}^N$ ,  $\epsilon > 0$ ,

$$(2.2) \quad \epsilon \frac{d}{d\tau} z = U(z, \epsilon),$$

where  $U$  is a sufficiently smooth function of  $z$  and  $\epsilon$ .

**Definition 2.2.** *The dynamical system (2.2) exhibits a fast-slow split if there is an  $\epsilon$ -dependent invertible transformation of the dependent variables into fast-slow coordinates  $(x, y)$ ,  $x \in \mathbb{R}^{N_x}$ ,  $y \in \mathbb{R}^{N_y}$ ,  $N = N_x + N_y$ , where the dynamics are described by a fast-slow system.*

In this paper, we restrict our attention to the *normally stable fast-slow system*, which is a fast-slow system where the fast directions are stable.

**Definition 2.3.** *A normally stable fast-slow system is a fast-slow system where the eigenvalues of the Jacobian,  $D_y f(x, y, 0) \in \mathbb{R}^{N_y \times N_y}$ , are strictly to the left of the imaginary axis when  $f(x, y, 0) = 0$ .*

Due to the dissipative fast-scale dynamics of normally stable fast-slow systems, the solutions will be attracted to an invariant slow manifold in forward time. We will now define the notion of the slow manifold for normally stable fast-slow systems. Consider a fast-slow system in the form (2.1).

**Lemma 2.4.** *For  $\epsilon > 0$  sufficiently small, there exists a function,  $y^*(x, \epsilon)$ , such that the graph*

$$(2.3) \quad M_\epsilon = \{(x, y) : y = y^*(x, \epsilon)\},$$

*is locally invariant under (2.1). We define  $M_\epsilon$  to be the slow manifold.*

This lemma is proved following Theorem 4 in [35]. The purpose of the FSNN is to be a universal approximator for normally stable fast-slow systems. The network is based on the following well known result due to Fenichel.

**Lemma 2.5.** *When  $\epsilon > 0$  is sufficiently small and  $(x, y)$  lies in a neighborhood around the slow manifold  $M_\epsilon$ , there exists a change of coordinates  $(x, y) \rightarrow (\tilde{x}, \tilde{y})$  where the dynamics of normally stable fast-slow systems can be written as,*

$$(2.4a) \quad \frac{d}{dt} \tilde{y} = A(\tilde{x}, \tilde{y}, \epsilon) \tilde{y},$$

$$(2.4b) \quad \frac{d}{dt} \tilde{x} = \epsilon \tilde{g}(\tilde{x}, \tilde{y}, \epsilon),$$

*where  $A(\tilde{x}, \tilde{y}, \epsilon) \in \mathbb{R}^{N_y \times N_y}$ ,  $\tilde{g}(\tilde{x}, \tilde{y}, \epsilon) \in \mathbb{R}^{N_x}$ , and  $A(\tilde{x}, 0, 0)$  is a stable matrix, i.e., its eigenvalues are on the left of the imaginary axis.*

The above lemma is derived in Chapter 3.2 of [35]. The lemma introduces (2.4), which is often called the *Fenichel normal form* due to the pioneer work of Neil Fenichel [21]. Note that the Fenichel normal form given in [35] is more general, including fixed points that are either stable or unstable in the linearization of the fast variable. In this work, we only consider fast variables

that are long-time stable. Moreover, due to the existence of the coordinate transformation, we consider the general form of the singularly perturbed systems (2.2). However, the advantage of the split form (2.1) is that the slow manifold dimension is known.

Our FSNN takes advantage of a modified formulation of Fenichel normal form which will be described in the following discussion. The following theorem forms the framework for the FSNN architecture.

**Theorem 2.6.** *Suppose the dynamics of  $z(t; \epsilon) \in \mathbb{R}^N$ ,  $\epsilon > 0$ , admit a fast-slow split and can be described by normally stable fast-slow system. Then there exists a  $\epsilon$ -dependent invertible transformation*

$$(2.5) \quad \begin{bmatrix} y \\ x \end{bmatrix} = h(z; \epsilon),$$

where  $x(t) \in \mathbb{R}^{N_x}$ ,  $y(t) \in \mathbb{R}^{N_y}$ , are slow and fast variables, respectively, and for  $|y| \leq \Delta$ , where  $\Delta > 0$ , the dynamics for  $(x, y)$  can be described using

$$(2.6a) \quad \frac{d}{dt}y = T(x)y + B(x, y, \epsilon)(y, y) + \epsilon C(x, y, \epsilon)y,$$

$$(2.6b) \quad \frac{d}{dt}x = \epsilon g(x, y, \epsilon).$$

$T(x) \in \mathbb{R}^{N_y \times N_y}$  is a block upper triangular matrix consisting of either  $\mathbb{R}^{2 \times 2}$  or  $\mathbb{R}$  blocks on the diagonal and the eigenvalues of these diagonal blocks are strictly to the left of the imaginary axis for all  $x$ .  $B(x, y, \epsilon) : \mathbb{R}^{N_y} \times \mathbb{R}^{N_y} \rightarrow \mathbb{R}^{N_y}$  is a bilinear map,  $C(x, y, \epsilon) \in \mathbb{R}^{N_y \times N_y}$  is a matrix, and  $g(x, y, \epsilon) \in \mathbb{R}^{N_x}$ .  $T$ ,  $B$ ,  $C$ , and  $g$  are smooth functions of their arguments.

In the following discussion, we will prove Theorem 2.6 by refining the Fenichel normal form in (2.4) and applying the matrix Schur decomposition. First, we modify (2.4) by performing a Taylor expansion of the term  $A(\tilde{x}, \tilde{y}, \epsilon)\tilde{y}$  about  $y = 0$  and  $\epsilon = 0$ . With sufficient smoothness on  $A$ , we have

$$(2.7) \quad A(\tilde{x}, \tilde{y}, \epsilon)\tilde{y} = A(\tilde{x}, 0, 0)\tilde{y} + B(\tilde{x}, \tilde{y}, \epsilon)(\tilde{y}, \tilde{y}) + \epsilon C(\tilde{x}, \tilde{y}, \epsilon)\tilde{y},$$

where  $B(\tilde{x}, \tilde{y}, \epsilon) : \mathbb{R}^{N_y} \times \mathbb{R}^{N_y} \rightarrow \mathbb{R}^{N_y}$  is a bilinear map and  $C(\tilde{x}, \tilde{y}, \epsilon) \in \mathbb{R}^{N_y \times N_y}$  are remainder terms. Next, the Schur decomposition of  $A(\tilde{x}, 0, 0)$  will be used to define a new set of fast coordinates.

**Definition 2.7.** *The Schur form of a matrix,  $A \in \mathbb{R}^{M \times M}$ , is a matrix  $T \in \mathbb{R}^{M \times M}$  that satisfies  $A = QTQ^T$ , where  $Q \in \mathbb{R}^{M \times M}$  is orthogonal ( $Q^T Q = I$ ) and  $T$  is block upper triangular where the diagonal blocks consist of  $\mathbb{R}$  and  $\mathbb{R}^{2 \times 2}$  blocks.*

**Lemma 2.8.** *The Schur decomposition of a matrix  $A \in \mathbb{R}^{M \times M}$ , is given by*

$$(2.8) \quad A = QTQ^T,$$

where  $Q, T \in \mathbb{R}^{M \times M}$ ,  $Q$  is an orthogonal matrix ( $Q^T Q = I$ ), and  $T$  is the Schur form of  $A$ . The eigenvalues of  $A$  are given by the eigenvalues of the diagonal blocks of  $T$ .

The existence of the Schur decomposition is proven in many references, including [30, 2], though for any given matrix, the decomposition is not unique. Let the Schur decomposition of  $A(\tilde{x}, 0, 0)$  be given by

$$(2.9) \quad A(\tilde{x}, 0, 0) = Q(\tilde{x})T(\tilde{x})Q(\tilde{x})^T,$$

where  $Q(\tilde{x}) \in \mathbb{R}^{N_y \times N_y}$  is an orthogonal matrix and  $T(\tilde{x}) \in \mathbb{R}^{N_y \times N_y}$  is the Schur form of  $A(\tilde{x}, 0, 0)$ . Due to our assumptions on  $A(\tilde{x}, 0, 0)$ , all of the eigenvalues of  $T(\tilde{x})$  are to the left of the imaginary axis. Consider the coordinate transformation  $\hat{y} = Q(\tilde{x})^T \tilde{y}$ . We form the relevant ODE for  $\hat{y}$  to use in place of the ODE for  $\tilde{y}$ .

$$\begin{aligned} \frac{d}{dt}\hat{y} &= Q(\tilde{x})^T \frac{d}{dt}\tilde{y} + (\nabla Q(\tilde{x})^T) \left( \frac{d}{dt}\tilde{x}, \tilde{y} \right) \\ &= Q(\tilde{x})^T Q(\tilde{x})T(\tilde{x})Q(\tilde{x})^T \tilde{y} + Q(\tilde{x})^T B(\tilde{x}, Q(\tilde{x})\hat{y}, \epsilon)(Q(\tilde{x})\hat{y}, Q(\tilde{x})\hat{y}) \\ &\quad + \epsilon Q(\tilde{x})^T C(\tilde{x}, \epsilon)Q(\tilde{x})\hat{y} + \epsilon (\nabla Q(\tilde{x})^T) (g_\epsilon(\tilde{x}, \hat{y}), \hat{y}). \\ &= T(\tilde{x})\hat{y} + Q(\tilde{x})^T B(\tilde{x}, Q(\tilde{x})\hat{y}, \epsilon)(Q(\tilde{x})\hat{y}, Q(\tilde{x})\hat{y}) \\ &\quad + \epsilon Q(\tilde{x})^T C(\tilde{x}, \epsilon)Q(\tilde{x})\hat{y} + \epsilon (\nabla Q(\tilde{x})^T) (g_\epsilon(\tilde{x}, \hat{y}), \hat{y}). \end{aligned}$$

By redefining terms, it can be shown that the ODE is equivalent to

$$\frac{d}{dt}\hat{y} = T(\tilde{x})\hat{y} + \tilde{B}(\tilde{x}, \hat{y}, \epsilon)(\hat{y}, \hat{y}) + \epsilon \tilde{C}(\tilde{x}, \hat{y}, \epsilon)\hat{y},$$

where  $\tilde{B}(\tilde{x}, \hat{y}, \epsilon)$  is a bilinear form operator and  $\tilde{C}(\tilde{x}, \hat{y}, \epsilon)$  is a matrix. This establishes an equivalence to (2.6).

Theorem 2.6 takes advantage of many useful properties. In the fast-slow coordinate system of Theorem 2.6, the definition of the slow-manifold simplifies significantly.

**Theorem 2.9.** *The graph,  $M = \{(x, y) : x \in \mathbb{R}^{N_x}, y = 0\}$  is locally invariant under (2.6).*

This theorem can be easily verified by substituting  $y = 0$  into (2.6a) and observing that  $\frac{d}{dt}y = 0$  on the slow manifold. Trajectories on the slow manifold will remain on the slow manifold for all time. In this case, the dynamics can be reduced to an ODE for the slow variable,

$$(2.10) \quad \frac{d}{d\tau}x = g(x, 0, \epsilon), \quad (x, y) \in M,$$

where  $\tau$  is the slow timescale. In the case when the coordinates  $(x, y)$  are close to, but not on  $M$ , the following theorem states that trajectories emanating from  $(x, y)$  will approach  $M$  exponentially in forward time.

**Theorem 2.10.** *If  $\epsilon > 0$  is sufficiently small, then, for  $|y| \leq \Delta$ , where  $\Delta > 0$ , there are  $\kappa > 0$  and  $\alpha < 0$  such that*

$$(2.11) \quad d((x(t), y(t)), M) \leq \kappa \exp(\alpha t),$$

where  $d$  represents the Euclidean distance.

This theorem is proved following Theorem 5 in [35].

Theorem 2.6 provides a framework for the FSNN architecture, which expresses each of the functions  $h, T, B, C$ , and  $g$  using neural networks with specially designed architectures described in the following section. There are a few considerations that went into using the modified Fenichel normal form. By expanding  $A(\tilde{x}, \tilde{y}, \epsilon)$  in (2.7), we expose three separate terms with known structures. We further use the Schur decomposition to explicitly expose the eigenvalues of  $A(\tilde{x}, 0, 0)$ , which are required to be left of the imaginary axis. Finally, we further simplify the linear term by absorbing the matrix  $Q(\tilde{x})$  into the representation. Though we use the Schur decomposition to represent  $A(\tilde{x}, 0, 0)$  in this paper, other decompositions for representing matrices with eigenvalues to the left of the imaginary axis have been studied in literature [19, 2].

**3. Fast-Slow Neural Networks (FSNNs).** In this section, we present a neural network-based approach to approximating the set of solutions to normally stable fast-slow systems using the framework of Theorem 2.6. We refer to this approach as the fast-slow neural network (FSNN), which is defined below and summarized in Figure 1.

**Definition 3.1.** *The fast slow neural network (FSNN) is a transformation of an initial condition,  $z_0$ , and parameter,  $\epsilon > 0$ , to a time series  $\{z_n\}_{n=0}^N$  corresponding to times  $t_0, \dots, t_N$ , where  $z_n \in \mathbb{R}^N$  for  $n = 0, \dots, N$ . The initial condition is transformed into fast-slow coordinates,  $(y_0, x_0)$ , via (2.5) where  $h$  is represented using an invertible coupling flow network. A numerical integration is used to approximate the solution to the fast-slow system in (2.6) to obtain the time series  $\{(y_n, x_n)\}_{n=0}^{N_t}$  for corresponding times  $t_0, \dots, t_N$ , where  $T$  is represented using a negative Schur form network,  $B$  is represented using a low-rank bilinear form network, and  $C$  and  $g$  are represented using feed-forward neural networks. The trajectories are then transformed back into the original coordinate system using*

$$(3.1) \quad z_n = h^{-1} \left( \begin{bmatrix} y_n & x_n \end{bmatrix}^T; \epsilon \right), \quad n = 1, \dots, N.$$

The key components of Definition 3.1, including the invertible coupling flow network, Schur form network, and low-rank bilinear form network, will be defined in the following sections. First we will begin by stating the main result of the paper.

**Theorem 3.2.** *The FSNN is a universal approximator for the set of solutions of normally stable fast-slow systems in the neighborhood of the slow manifold.*

Due to Theorem 2.6, normally stable fast-slow systems can be represented using (2.5)–(2.6). Therefore, the FSNN inherits the universal approximation properties of its components, which we will later show are universal approximators for their corresponding class of functions. The invertible coupling flow network which represents  $h$  is described in Section 3.1 and was proven to be a universal approximator to invertible maps in [58]. The universal approximation theorems of the negative Schur form network representing  $T$  and the bilinear form network representing  $B$  are proved in Sections 3.2 and 3.3, respectively. The universal approximation of nonlinear functions using feedforward neural networks for  $C$  and  $g$  are well known, e.g. [15]. Finally, we describe a consistent numerical scheme to obtain trajectories in time, which has an error bound that vanishes as the time steps  $\Delta t_n = t_n - t_{n-1} \rightarrow 0$ .



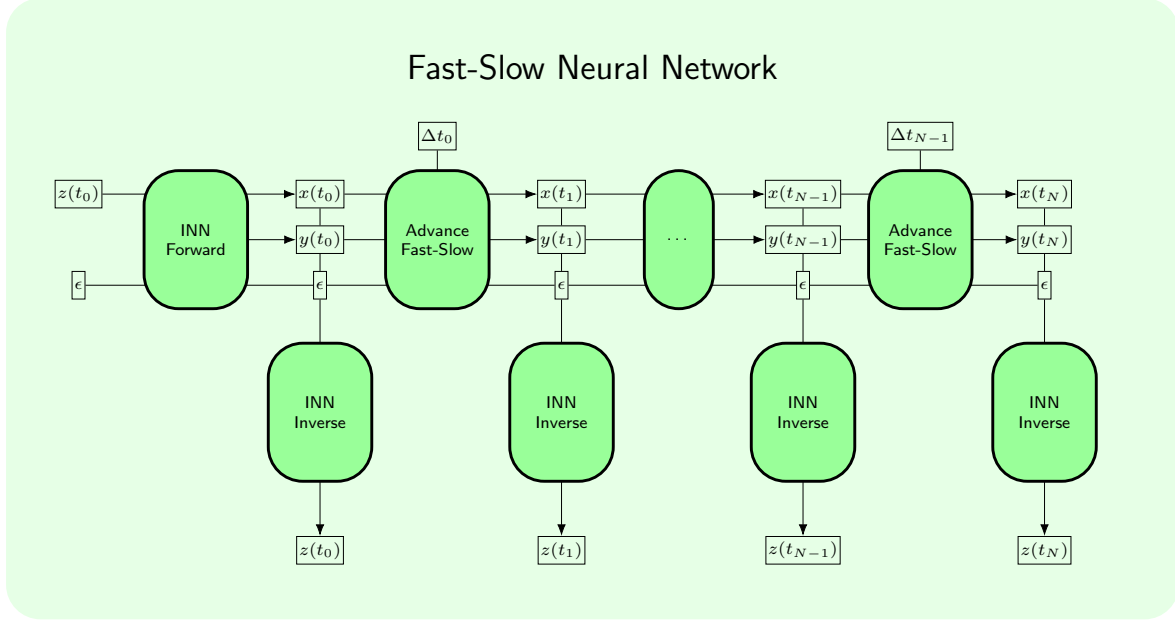


**Figure 1.** Schematic of the fast-slow neural network (FSNN). The original coordinates are projected into fast-slow coordinates using the invertible neural network (INN). In these coordinates, numerical integration is used to advance the solution to later time steps. The inverse function of the INN is used to convert the fast-slow coordinates into the original coordinate system.

Our ML-based approach naturally comes with a set of hyperparameters. The standard hyperparameters are those related to the architectures of  $h$ ,  $T$ ,  $C$  and  $g$ . The only systemic hyperparameters are the dimensions of the slow and fast subspaces,  $N_x$  and  $N_y$ , respectively. In the examples considered in Section 5, the true dimensions of slow manifolds are known and used. In applications when the size of the slow manifold dimension is not known, tools like diffusion maps [13] or proper orthogonal decomposition (POD) [5] may be used to infer the size of the reduced dimension before applying the proposed FSNN.

**3.1. The Invertible Coupling Flow Network.** Now we will describe further details of the FSNN architecture. The first component is the invertible function,  $h(z; \epsilon)$ , which represents the transformation into fast-slow coordinates. The network is based on the invertible coupling flow network developed in [1], where the authors closely follow the architecture provided by [18]. These networks have been shown to be universal approximators to invertible functions in [58]. In this work, we modify the original network by introducing a regularization property which controls the Lipschitz constant of both the forward and inverse map. Such a regularization improves the robustness of the network during training. The constant is a tunable parameter of the network that, similar to the hidden dimensions of the network, can be made arbitrarily large to increase the expressiveness of the network. Therefore, this modification is compatible with the universal approximation result derived in [58]. As such, we introduce the key ingredient of Lipschitz control.



**Definition 3.3.** The bi-Lipschitz affine transformation (bLAT) layer is given by the transformation,  $f : \mathbb{R}^N \rightarrow \mathbb{R}^M$ , defined by

$$(3.2) \quad f(x) = U\Sigma V^T x + b,$$

where  $U \in \mathbb{R}^{M \times r}$ ,  $V \in \mathbb{R}^{r \times N}$ ,  $\Sigma \in \mathbb{R}^{r \times r}$ ,  $b \in \mathbb{R}^M$ ,  $r = \min(M, N)$ ,  $U$  and  $V$  are orthogonal matrices satisfying  $U^T U = V^T V = I$ , and

$$(3.3) \quad \Sigma = \text{diag} \begin{bmatrix} \sigma_1 & \dots & \sigma_r \end{bmatrix},$$

where  $\frac{1}{L} \leq \sigma_i \leq L$  for  $i = 1, \dots, r$  and some  $L \geq 1$ . When  $M = N$ , the mapping is invertible.

$$(3.4) \quad f^{-1}(x) = V\Sigma^{-1}U^T(x - b).$$

Our new contribution is to include the matrix term  $U\Sigma V^T$ , which is written as a singular value decomposition (SVD), which exists for every matrix in  $\mathbb{R}^{M \times N}$ . One advantage of the bLAT layer is the following theorem.

**Theorem 3.4.** The forward and inverse bLAT layers are both  $L$ -bi-Lipschitz.

This follows from the fact that  $\frac{1}{L} \leq \|\nabla f(x)\|_2 \leq L$  and  $\frac{1}{L} \leq \|\nabla f^{-1}(x)\|_2 \leq L$ . Another advantage of using the SVD is that, by construction, the evaluation of  $f(x)$  and  $f^{-1}(x)$  have an equivalent computational cost. In our implementation of the  $M = N$  case, the orthogonal matrices of the bLAT layers are parameterized using the matrix exponential of a skew-symmetric matrix input, i.e.  $U = \expm(S)$ , where  $S = -S^T$ . When  $M \neq N$ , the orthogonal matrices are parameterized using the Householder factorization.

The second component of the invertible coupling flow network is the affine coupling flow layer, defined below. We introduce a similar regularization idea to the above.

**Definition 3.5.** The affine coupling flow layer is defined by the transformation  $y = f(x)$ ,  $x, y \in \mathbb{R}^M$ , which is implicitly defined by

$$(3.5) \quad \begin{bmatrix} y_1 \\ y_2 \end{bmatrix} = \begin{bmatrix} \text{diag}(F(x_2)) & \\ & \text{diag}(G(y_1)) \end{bmatrix} \begin{bmatrix} x_1 \\ x_2 \end{bmatrix} + \begin{bmatrix} B(x_2) \\ C(y_1) \end{bmatrix},$$

where  $x = \begin{bmatrix} x_1 & x_2 \end{bmatrix}^T$ ,  $y = \begin{bmatrix} y_1 & y_2 \end{bmatrix}^T$ ,  $x_1, y_1 \in \mathbb{R}^d$ ,  $x_2, y_2 \in \mathbb{R}^{M-d}$ ,  $F, B : \mathbb{R}^{M-d} \rightarrow \mathbb{R}^d$ ,  $G, C : \mathbb{R}^d \rightarrow \mathbb{R}^{M-d}$ ,  $1 \leq d < M$  and the range of the output elements of  $F$  and  $G$  is constrained to  $[\frac{1}{L}, L]$  for some  $L \geq 1$ . The inverse mapping,  $x = f^{-1}(y)$ , is implicitly defined by

$$(3.6) \quad \begin{bmatrix} x_1 \\ x_2 \end{bmatrix} = \begin{bmatrix} \text{diag}(F(x_2))^{-1} & \\ & \text{diag}(G(y_1))^{-1} \end{bmatrix} \left( \begin{bmatrix} y_1 \\ y_2 \end{bmatrix} - \begin{bmatrix} B(x_2) \\ C(y_1) \end{bmatrix} \right).$$

The functions  $F, G, B, C$  are represented using feed-forward neural networks. In order to constrain outputs to the range  $[\frac{1}{L}, L]$ , we apply the map  $\theta_L : \mathbb{R} \rightarrow [\frac{1}{L}, L]$  defined by  $\theta_L(s) = \exp(\log(L) \tanh(s))$ . This constraint ensures invertibility of the affine coupling layer. The Lipschitz constant is a function of  $L$  and  $\nabla F, \nabla G, \nabla B, \nabla C$  and can optionally be constrained using bLAT layers in the feedforward networks.

The invertible coupling flow network combines bLAT layers and affine coupling flow layers into a network.

**Definition 3.6.** Let  $f_1, \dots, f_K : \mathbb{R}^M \rightarrow \mathbb{R}^M$  define a set of bLAT layers and  $g_1, \dots, g_K : \mathbb{R}^M \rightarrow \mathbb{R}^M$  define a set of affine coupling flow layers. The invertible coupling flow network,  $h : \mathbb{R}^M \rightarrow \mathbb{R}^M$  is defined as the composition

$$(3.7) \quad h = g_K \circ f_K \circ \dots \circ g_1 \circ f_1$$

and the inverse map is defined by

$$(3.8) \quad h^{-1} = f_1^{-1} \circ g_1^{-1} \circ \dots \circ f_K^{-1} \circ g_K^{-1}.$$

The free parameter  $L$  in each of the layers adjusts the complexity of the overall network and can be used as an effective regularizer. Despite the introduction of this regularization parameter, the network can be made arbitrarily expressive with the tuning of  $L$ , and therefore the universal approximation result from [58] still holds true.

**Theorem 3.7.** The invertible coupling flow network is a universal approximator for invertible maps.

In Theorem 2.6, the invertible transformation is  $\epsilon$ -dependent. Therefore, we bake this dependence into the network by including  $\epsilon$  as a functional dependence in  $F, G, B, C$ .

**3.2. The Negative Schur Form Network.** Next, a parameterization suitable for representing  $T$  is discussed. We present the negative Schur form network, which is a differentiable parameterization for Schur forms with eigenvalues to the left of the imaginary axis. The Schur form network is composed of a feedforward neural network in which the outputs are re-formatted into a negative Schur form matrix, which is defined below.

**Definition 3.8.** The negative Schur form matrix is given by the block matrix  $T \in \mathbb{R}^{N_y \times N_y}$ , where

$$(3.9) \quad T = \begin{bmatrix} T_{11} & T_{12} & \dots & T_{1p} \\ & T_{22} & \dots & T_{2p} \\ & & \ddots & \vdots \\ & & & T_{pp} \end{bmatrix}.$$

When  $M$  is even,  $p = M/2$  and  $T_{ij} \in \mathbb{R}^{2 \times 2}$  for  $i = 1, \dots, p$ ,  $j = i, \dots, p$ . When  $M$  is odd,  $p = (M + 1)/2$ ,  $T_{ij} \in \mathbb{R}^{2 \times 2}$  for  $i = 1, \dots, p - 1$ ,  $j = i, \dots, p - 1$ ,  $T_{ip} \in \mathbb{R}^2$  for  $i = 1, \dots, p - 1$ , and  $T_{pp} \in (-\infty, 0)$ . Each of the  $\mathbb{R}^{2 \times 2}$  blocks on the diagonal are further parameterized using the map

$$(3.10) \quad \mathcal{M}(R, r, \theta, \phi) = R \begin{bmatrix} \cos(\theta) & \sin(\theta) \\ -\sin(\theta) & \cos(\theta) \end{bmatrix} + r \begin{bmatrix} \cos(\phi) & \sin(\phi) \\ \sin(\phi) & -\cos(\phi) \end{bmatrix},$$

where the region of parameters is restricted to

$$(3.11) \quad |R| \geq |r|, \quad R < 0, \quad \theta \in \left(-\frac{\pi}{2}, \frac{\pi}{2}\right).$$

Due to this parameterization, we have the following theorem.

**Theorem 3.9.** *The negative Schur form network is a parameterization for the set of Schur forms with eigenvalues to the left of the imaginary axis.*

This can be proven by showing that (3.10)–(3.11) can smoothly represent both complex conjugate pairs and real pairs of eigenvalues with negative real part. Equation (3.10) represents the  $\mathbb{R}^{2 \times 2}$  matrix as a 4-parameter family sum of a symmetric and antisymmetric operator [6]. Let  $m = \frac{1}{2}\text{Tr}(\mathcal{M}) = R \cos(\theta)$  and  $p = \det(\mathcal{M}) = R^2 - r^2$ . Then the eigenvalues of  $\mathcal{M}$  are given by

$$(3.12) \quad \lambda_{\pm} = m \pm \sqrt{m^2 - p}.$$

The real parts of the eigenvalues are given by

$$(3.13) \quad \text{Re}(\lambda_{\pm}) = m \pm \sqrt{\max(m^2 - p, 0)}.$$

Figure 2 shows the regions of the  $m$ – $p$  plane where both eigenvalues are less than zero (green region), greater than zero (red region), complex (blue region), and real (outside of the blue region). In order for  $\text{Re}(\lambda_{\pm}) < 0$ , we must have  $m < 0$  and  $p > 0$ . This translates to the constraints in (3.11).

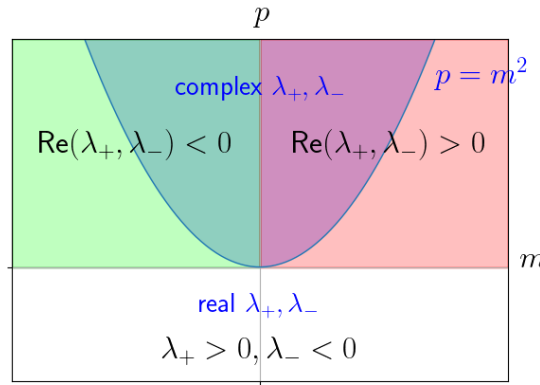


**Figure 2.** Plot showing the eigenvalues encountered in various regions of the  $m$ – $p$  plane, where  $m = \frac{1}{2}\text{Tr}(\mathcal{M}) = R \cos(\theta)$  and  $p = \det(\mathcal{M}) = R^2 - r^2$ . The green region corresponds to linear stability,  $\text{Re}(\lambda_{+}, \lambda_{-}) < 0$ , and the red region corresponds to linear instability,  $\text{Re}(\lambda_{+}, \lambda_{-}) > 0$ . Above the parabola  $p = m^2$  (in the blue region), eigenvalues are complex. Below the parabola (outside of the blue region), the eigenvalues are real.

In the implementation of the network, each of the  $\mathbb{R}^{2 \times 2}$  blocks have four tunable parameters,  $\bar{R}, \bar{r}, \bar{\theta}, \bar{\phi} \in \mathbb{R}$ , that are mapped onto the restricted domain using

$$(3.14) \quad R = -|\bar{r}|e^{|\bar{R}|}, \quad r = \bar{r}, \quad \theta = \frac{\pi}{2} \tanh(\bar{\theta}), \quad \phi = \bar{\phi}.$$

The remaining off-diagonal terms are unrestricted in parameter space. In order to achieve dependence with respect to  $x$ , (i.e.  $T(x)$ ), we introduce a feedforward network which takes  $x$  as an input and outputs both the tunable parameters  $\bar{R}, \bar{r}, \bar{\theta}, \bar{\phi}$  for each diagonal block and the elements of the remaining blocks. The resulting negative Schur form matrix is returned as the output of  $T(x)$ .

**3.3. The Low-Rank Bilinear Form Network.** Finally, we introduce an approximation for the bilinear form term,  $B$ .

**Definition 3.10.** *The low-rank bilinear form network  $B : \mathbb{R}^{N_x} \times \mathbb{R}^{N_y} \rightarrow \mathbb{R}^{N_z}$  is defined by*

$$(3.15) \quad B(x, y) = \sum_{r=1}^R (C^{(r)}x) \odot (D^{(r)}y),$$

where  $x \in \mathbb{R}^{N_x}$ ,  $y \in \mathbb{R}^{N_y}$ ,  $C^{(r)} \in \mathbb{R}^{N_z \times N_x}$ ,  $D^{(r)} \in \mathbb{R}^{N_z \times N_y}$ ,  $\odot$  represents the Hadamard product (element-wise multiplication), and  $R$ ,  $1 \leq R \leq \min(N_x, N_y)$ , represents the rank of approximation.

Here,  $R$  is a tunable parameter. Increasing  $R$  gives more expressive power at the expense of computational cost. This network has the following property:

**Theorem 3.11.** *The low-rank bilinear form network is a universal approximator to the set of bilinear forms.*

Consider the bilinear form,  $\tilde{B} : \mathbb{R}^{N_x} \times \mathbb{R}^{N_y} \rightarrow \mathbb{R}^{N_z}$ . We can represent the operator of this function as  $\tilde{B}_{ijk}$  where  $B_i \in \mathbb{R}^{N_x \times N_y}$  for  $i = 1, \dots, N_z$ . Let  $p = \min(N_x, N_y)$ , then we can use the singular value decomposition to represent the matrix  $\tilde{B}_i$  as

$$(3.16) \quad \tilde{B}_i = \sum_{r=1}^p \sigma_i^{(r)} u_i^{(r)} (v_i^{(r)})^T,$$

where  $\sigma_i^{(r)}$ ,  $u_i^{(r)}$ ,  $v_i^{(r)}$ ,  $r = 1, \dots, p$ , are the singular values, left singular vectors, and right singular vectors of  $\tilde{B}_i$ , respectively, and  $\sigma_1 \geq \dots \geq \sigma_p \geq 0$ . The  $i^{\text{th}}$  term of  $\tilde{B}(x, y)$  is given by

$$(3.17) \quad x^T \tilde{B}_i y = \sum_{r=1}^p \sigma_i^{(r)} x^T u_i^{(r)} (v_i^{(r)})^T y = \sum_{r=1}^p \sigma_i^{(r)} \left( \sum_{j=1}^{N_x} u_{ij}^{(r)} x_j \right) \left( \sum_{k=1}^{N_y} v_{ik}^{(r)} y_k \right),$$

We can find some  $C \in \mathbb{R}^{N_z \times N_x}$  and  $D \in \mathbb{R}^{N_z \times N_y}$  such that

$$(3.18) \quad x^T \tilde{B}_i y = \sum_{r=1}^p \left( \sum_{j=1}^{N_x} C_{ij}^{(r)} x_j \right) \left( \sum_{k=1}^{N_y} D_{ik}^{(r)} y_k \right).$$

This is equivalent to

$$(3.19) \quad \tilde{B}(x, y) = \sum_{r=1}^p (C^{(r)}x) \odot (D^{(r)}y).$$

The network uses a truncated version of this sum to approximate the action of the bilinear operator. The approximation error of the low-rank bilinear form network is  $\|B_i - \tilde{B}_i\|_2 = \sigma_i^{(R+1)}$ . This error can be decreased by increasing  $R$ .

In our formulation, the operator  $B$  has coefficients which are functions of  $x, y$ , and  $\epsilon$ . We inject this functional dependence by making the elements of  $C^{(r)}$  and  $D^{(r)}$  outputs of a feed-forward network with inputs  $(x, y, \epsilon)$ .

**3.4. Numerical Integration.** The Schur form,  $T$  will have eigenvalues that can be of arbitrarily large magnitude. Due to this, the dynamics of (2.6) will be stiff. Therefore, an Implicit-Explicit (IMEX) time integrator can be used to solve (2.6) efficiently. The IMEX scheme has been applied to a neural ODE framework in [62]. As shown below, an additional benefit of the proposed FSNN is to eliminate the need for iterative or direct linear solvers, thereby simplifying the training process.

Consider an IMEX Runge-Kutta method consisting of a diagonally implicit for treating the stiff linear term and an explicit method for treating the nonlinear term. The method can be represented by the following Butcher tableau.

$$\begin{array}{ccc|ccc} a_{11} & & & & & & \\ a_{21} & a_{22} & & & \alpha_{21} & & \\ \vdots & \vdots & \ddots & & \vdots & \ddots & \\ a_{s1} & \dots & \dots & a_{ss} & \alpha_{s1} & \dots & \alpha_{s,s-1} \\ \hline b_1 & \dots & \dots & b_s & \beta_1 & \dots & \beta_{s-1} & \beta_s \end{array}$$

Let  $x_n \approx x(t_n)$ ,  $y_n \approx y(t_n)$ , and  $\Delta t = t_n - t_{n-1}$ . Let  $f(x, y, \epsilon) = B(x, y, \epsilon)(y, y) + \epsilon C(x, y, \epsilon)y$ . The intermediate stages are implicitly defined by

$$(3.20a) \quad X^i = x_{n-1} + \epsilon \Delta t \sum_{j=1}^{i-1} \alpha_{ij} g(X^j, Y^j, \epsilon),$$

$$(3.20b) \quad Y^i = y_{n-1} + \Delta t \sum_{j=1}^i a_{ij} T(X^j) Y^j + \Delta t \sum_{j=1}^{i-1} \alpha_{ij} f(X^j, Y^j, \epsilon)$$

for  $i = 1, \dots, s$ . The above equation can be written to expose the linear system that needs to be solve.

$$(3.21) \quad Y^i = (I - \Delta t a_{ii} T(X^i))^{-1} \left( y_{n-1} + \Delta t \sum_{j=1}^{i-1} (a_{ij} T(X^j) Y^j + \alpha_{ij} f(X^j, Y^j, \epsilon)) \right)$$

Note that the matrix given by  $I - \Delta t a_{ii} T(X^i)$  is a block 2-by-2 upper triangular matrix. Due to the proposed architecture, this inverse can be handled efficiently using a backward substitution solve. Since  $T$  additionally has functional dependence, we treat this in a vectorization-friendly matrix-free fashion, which avoids storing multiple matrices  $T(X^i)$  for each data pair in the batch set during training. The solution at the next time step is obtained through the update

$$(3.22a) \quad x_n = x_{n-1} + \epsilon \Delta t \sum_{i=1}^s \beta_i g(X^i, Y^i, \epsilon),$$

$$(3.22b) \quad y_n = y_{n-1} + \Delta t \sum_{i=1}^s (b_i T(X^i) Y^i + \beta_i f(X^i, Y^i, \epsilon)).$$

In our implementation, we use the two-stage second-order accurate IMEX strong-stability-preserving L-stable scheme defined in [49].

When the solution is initially on the slow manifold ( $y = 0$ ), the stages  $Y^i$  for  $i = 1, \dots, s$  evaluate exactly to zero and therefore the numerical scheme can be simplified to an integration of the slow variables given by

$$(3.23a) \quad x_n = x_{n-1} + \epsilon \Delta t \sum_{i=1}^s \beta_i g(X^i, 0, \epsilon),$$

$$(3.23b) \quad X^i = x_{n-1} + \epsilon \Delta t \sum_{j=1}^{i-1} \alpha_{ij} g(X^j, 0, \epsilon), \quad i = 1, \dots, s.$$

In this case, one can take larger time steps (e.g.  $\Delta t \sim \frac{1}{\epsilon}$ ) and step over the fast dynamics formally. A hybrid scheme can also be used where the full system in (3.22) can be integrated until  $\|y\|$  is sufficiently small, after which slow integration in (3.23) is pursued using larger time steps. We note that some of the first works to use Runge-Kutta based residual networks to learn equations from time series was pursued in [51, 50].

**Data-driven closure.** A closure discovery procedure is implied through the above integration with large time steps. For a given full state vector  $z_0$ , the transformation  $h$  first maps to the separate state of  $(x_0, y_0)$ . The state vector is then projected onto the closure of  $y = 0$ ; the system for  $x$  is thus closed and evolved using (3.23). Finally, the evolved state of  $x$  is lifted back to the full state  $z$  using  $h^{-1}$ .

**4. Numerical Implementation.** In this section, we describe the numerical implementation of the fast-slow neural network and its corresponding training algorithm. The computation of the loss function and its gradient is summarized in Figure 3. The training set consists of both trajectory data, which describes the behavior of the dynamics, and manifold data, which describes the limiting behavior of the system. The trajectory dataset,  $\mathcal{D}$ , contains time series,  $\{(t_n^{(k)}, z_n^{(k)})\}_{n=1}^{N_t}$ , and parameters  $\epsilon^{(k)}$ , for  $k = 1, \dots, N_d$ , where  $N_d$  is the number of trajectory data samples. The manifold dataset,  $\mathcal{M}$ , contains multiple examples of the solution on the slow manifold,  $z^{(k)}$ , with corresponding parameters  $\epsilon^{(k)}$ , for  $k = 1, \dots, N_m$ . Examples of manifold data can be obtained either experimentally by integrating a model for a sufficiently long time with a small  $\epsilon$  or analytically if the equations permit an  $\epsilon = 0$  reduction or asymptotic expansion.

The loss function is given by

$$(4.1) \quad \mathcal{L} = \mathcal{L}_{\text{system}} + \mathcal{L}_{\text{fast}} + \mathcal{L}_{\text{slow}} + \mathcal{L}_{\text{manifold}}.$$

The first three terms are evaluated using the trajectory data set,  $\mathcal{D}$ , and the last term is evaluated using the manifold data set,  $\mathcal{M}$ . For the dynamics-oriented loss terms, the fast-slow neural network is applied to initial conditions in  $\mathcal{D}$  to obtain the model trajectories,  $\{(t_n^{(k)}, \tilde{x}_n^{(k)}, \tilde{y}_n^{(k)}, \tilde{z}_n^{(k)})\}$ . Additionally, the invertible coupling flow network is applied to the trajectory in  $\mathcal{D}$  to augment the data  $\{(t_n^{(k)}, x_n^{(k)}, y_n^{(k)}, z_n^{(k)})\}$ . Let  $L$  be an operator representing the approximation to the time integral of squared error, given by

$$(4.2) \quad L(t, z, \tilde{z}) = \sum_{n=0}^{N_t-1} \frac{1}{2} ((z_{n+1} - \tilde{z}_{n+1})^2 + (z_n - \tilde{z}_n)^2) (t_{n+1} - t_n).$$

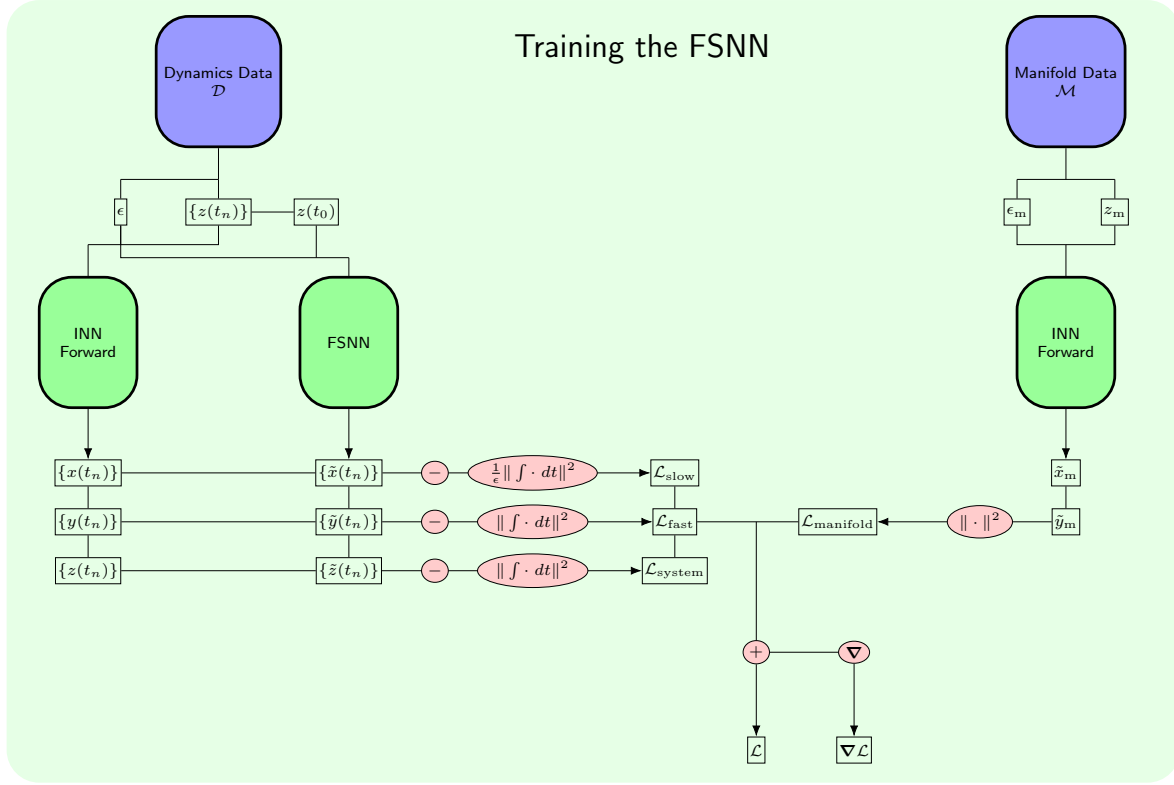


**Figure 3.** Schematic of training the fast-slow neural network (FSNN). The network is trained on dynamics data,  $\mathcal{D}$ , which contains examples of trajectories on both the fast and slow timescales and manifold data,  $\mathcal{M}$ , which contains examples of solution vectors that lie on the slow manifold. The overall loss is a combination of the dynamics loss, which includes  $L_2$  losses in the original coordinates ( $\mathcal{L}_{\text{system}}$ ), fast coordinates ( $\mathcal{L}_{\text{fast}}$ ), and slow coordinates ( $\mathcal{L}_{\text{slow}}$ ), and the manifold loss ( $\mathcal{L}_{\text{manifold}}$ ), which is an  $L_2$  loss of the fast coordinate, which should map to  $y = 0$  on the slow manifold.

Then we choose

$$(4.3a) \quad \mathcal{L}_{\text{system}} = \frac{1}{N_d} \sum_{k=1}^{N_d} L(t, z^{(k)}, \tilde{z}^{(k)}),$$

$$(4.3b) \quad \mathcal{L}_{\text{fast}} = \frac{1}{N_d} \sum_{k=1}^{N_d} L(t, y^{(k)}, \tilde{y}^{(k)}),$$

$$(4.3c) \quad \mathcal{L}_{\text{slow}} = \frac{1}{\epsilon^{(k)} N_d} \sum_{k=1}^{N_d} L(t, x^{(k)}, \tilde{x}^{(k)}).$$

Including the three terms individually encourages the network to learn the dynamics for the original and fast-slow coordinates to an adequate level.

In practice, we split the trajectory dataset,  $\mathcal{D}$ , into a fast-scale subset, with time steps chosen to smoothly capture the fast dynamics converging to the slow manifold, and a slow-



scale subset, with larger time steps chosen to capture the variation of the slow variables after the dynamics sufficiently close to the slow manifold. The trajectories in fast-scale subset are treated using the full integration in (3.22) while the trajectories from the slow-scale subset are treated using the slow-manifold integration in (3.23).

For the manifold loss term, the invertible coupling flow network is applied to examples in  $\mathcal{M}$  to obtain fast-slow coordinates  $(x^{(k)}, y^{(k)})$ . If the data is on the slow manifold, then  $y^{(k)}$  should be zero. We therefore include the following as a penalty term.

$$(4.4) \quad \mathcal{L}_{\text{manifold}} = \frac{1}{N_m} \sum_{k=1}^{N_m} (y^{(k)})^2$$

Our implementation of the fast-slow neural network uses Jax [7] as a backend. Auto-differentiation is used to compute gradients of the loss function with respect to the tunable parameters and the Adam optimizer from the Optax [17] package is used adjust the weights towards an locally optimal solution for the dataset.

**5. Examples.** In this section, we consider multiple example problems to demonstrate the applicability of the FSNN to various problems, including multi-scale problems arising in hydrodynamics, climate dynamics, and plasma physics.

**5.1. Visualization of the Attracting Slow Manifold Property.** A significant advantage of the FSNN is that, for any choice of model parameters, the network will have an attracting slow manifold that, due to Theorem 2.6, will attract solutions for sufficiently small values of  $\epsilon$ . The slow manifold is represented by the graph,  $y = 0$ . In Figure 4, we demonstrate this property on multiple random initializations of FSNNs for  $N_y = N_x = 1$ . Initial conditions are drawn randomly from a standard normal distribution (left plot) and are integrated to a later time  $t = 4$ . The trajectory points at  $t = 4$  (blue dots) and the resulting slow manifold (orange curves) are plotted at this final time, demonstrating convergence of solutions to the slow manifold.

**5.2. Learning a Simple Attracting Manifold.** We demonstrate the ability of the FSNN to learn dynamics for a simple test problem where the dynamics can be described by the following system of ODEs for  $z_1, z_2 \in \mathbb{R}$ .

$$(5.1a) \quad \frac{dz_1}{dt} = -\epsilon(\sin(z_1) + z_2)$$

$$(5.1b) \quad \frac{dz_2}{dt} = \lambda(z_1)(z_2 - \theta(z_1))$$

In this example,  $z_1$  represents the slow variable and  $z_2$  represents the fast variable. When  $\epsilon = 0$ , the slow manifold is given by  $\theta(z_1)$ . In this example, we choose  $\lambda$  and  $\theta$  to be

$$(5.2) \quad \lambda(x) = -1 - \frac{1}{10} \cos(2x), \quad \theta(x) = 2 \tanh(x).$$

The trajectory dataset,  $\mathcal{D}$ , consists of  $10^3$  fast-scale trajectories, corresponding to initial conditions for  $z_1, z_2$  randomly generated uniformly in  $[-1, 1]$ ,  $\epsilon$  randomly generated log-uniformly in  $[10^{-5}, 10^{-2}]$ , and integrated forward 5 timesteps using an adaptive RK45 solver

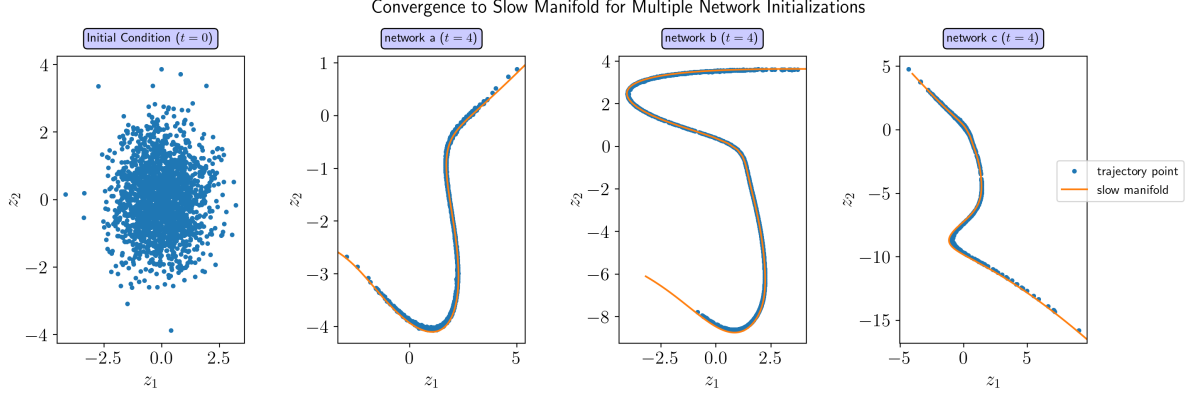


**Figure 4.** Demonstration of attracting slow manifold property of the FSNN. For three different random initializations of the FSNN, initial conditions are drawn randomly from a standard normal distribution and are evolved in time to a later time ( $t = 4$ ). The dynamics are shown to limit to the curve representing the slow manifold.

with an error tolerance of  $10^{-8}$ . The manifold dataset,  $\mathcal{M}$ , consists of  $10^3$  examples of data pairs  $((z_1, z_2), \epsilon = 0)$  on the graph  $z_2 = \theta(z_1)$ , where  $z_1$  is randomly generated uniformly in  $[-1, 1]$ .

A FSNN is trained on this dataset using the Adam optimizer from Optax. The INN consists of one outer layer, where the inner coupling flow layers consists of feedforward networks with one layer and a hidden dimension of 10. East of the feedforward neural networks on the RHS of the neural ODE system consists of 10 layers and the bilinear form has a rank of 2.

Figure 5 shows a comparison of the trained model and the reference solution in phase space for various choices of  $\epsilon$ . The model shows great agreement to the reference solution. In all of the plots, it is evident that the trajectories eventually get trapped in a slow manifold. In the rightmost plot, a comparison of the learned eigenvalues with that of the ground truth,  $\lambda(z_1)$ , is shown. The results demonstrate that the FSNN is able to successfully recover details of the original operator.

**5.3. Grad's Moment System.** In this example, we show that the FSNN can be applied towards learning hydrodynamic slow manifolds. We consider a linear Grad moment system [26, 27], defined by

$$(5.3a) \quad \partial_t \rho = -\epsilon \nabla \cdot \mathbf{u},$$

$$(5.3b) \quad \partial_t \mathbf{u} = -\epsilon (\nabla \rho + \nabla T + \nabla \cdot \sigma),$$

$$(5.3c) \quad \partial_t T = -\frac{2\epsilon}{3} (\nabla \cdot \mathbf{u} + \nabla \cdot \mathbf{q}),$$

$$(5.3d) \quad \partial_t \sigma = -\sigma - \epsilon \left( 2 \overline{\nabla \mathbf{u}} + \frac{4}{5} \overline{\nabla \mathbf{q}} \right),$$

$$(5.3e) \quad \partial_t \mathbf{q} = -\frac{2}{3} \mathbf{q} - \epsilon \left( \frac{5}{2} \nabla T + \nabla \cdot \sigma \right),$$

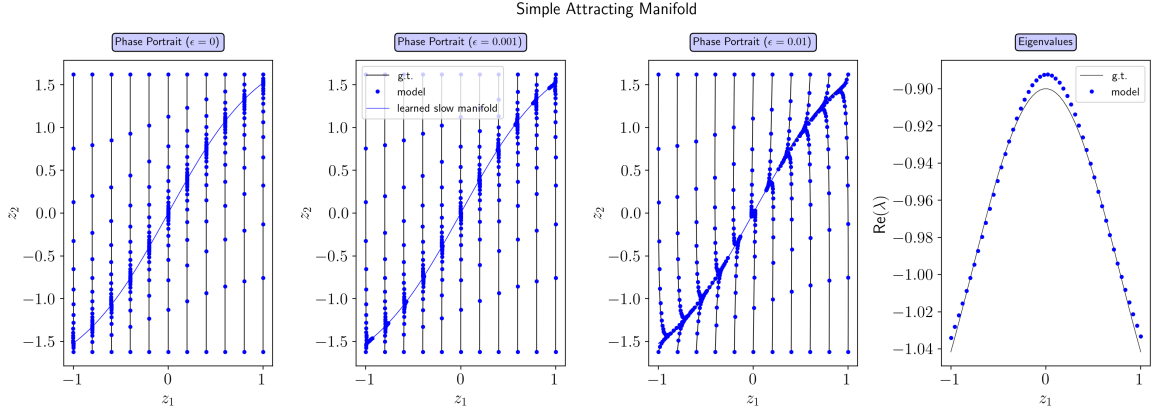


**Figure 5.** Results of learning the dynamics of the simple attracting manifold example described by (5.1). Left three plots: phase portraits comparing the ground truth (g.t.) reference solution (bold curves) and that of the trained model (dots) for  $\epsilon = 0, 0.001, 0.01$ . Rightmost plot: comparison of the eigenvalues learned by the FSNN with the ground truth eigenvalues.

where  $\rho(\mathbf{x}, t)$  is the density,  $\mathbf{u}(\mathbf{x}, t)$  is velocity,  $T(\mathbf{x}, t)$  is temperature,  $\sigma(\mathbf{x}, t)$  is the stress tensor,  $\mathbf{q}(\mathbf{x}, t)$  is the heat flux, and  $\mathbf{x} = (x, y, z)^T \in \mathbb{R}^3$  is the spatial coordinate. The overline represents the symmetric, traceless part of a tensor, e.g.

$$(5.4) \quad \bar{\mathbf{a}} = \frac{1}{2}(\mathbf{a} + \mathbf{a}^T) - \frac{1}{3}\mathbf{I}\text{Tr}(\mathbf{a}).$$

We consider solutions that are one-dimensional ( $\partial_y = \partial_z = 0$ ) and  $2\pi$ -periodic in space, e.g.

$$(5.5) \quad \rho(\mathbf{x}, t) = \sum_{k=-\infty}^{\infty} \rho_k(t) e^{ikx}.$$

The Fourier coefficients are governed by the following system of ODEs.

$$(5.6) \quad \frac{d}{dt} \begin{bmatrix} \rho_k \\ u_k \\ T_k \\ \sigma_k \\ q_k \end{bmatrix} = \begin{bmatrix} 0 & -ik\epsilon & 0 & 0 & 0 \\ -ik\epsilon & 0 & -ik\epsilon & -ik\epsilon & 0 \\ 0 & -\frac{2}{3}ik\epsilon & 0 & 0 & -\frac{2}{3}ik\epsilon \\ 0 & -\frac{4}{3}ik\epsilon & 0 & -1 & -\frac{8}{15}ik\epsilon \\ 0 & 0 & -\frac{5}{2}ik\epsilon & -ik\epsilon & -\frac{2}{3} \end{bmatrix} \begin{bmatrix} \rho_k \\ u_k \\ T_k \\ \sigma_k \\ q_k \end{bmatrix}, \quad k = 0, \pm 1, \dots$$

For this example, we truncate the Fourier series to consider only the  $k = 0, \pm 1, \pm 2$  models. Initial conditions are randomly generated for each Fourier coefficient uniformly in the complex region  $[-1, 1] \times [-i, i]$ . The solution is computed for 10 time steps both using  $\Delta t_{\text{fast}} = \frac{1}{4}$  and  $\Delta t_{\text{slow}} = \frac{1}{4\epsilon}$ . The slow-scale trajectories are offset  $\Delta t_{\text{slow}}$  from  $t = 0$  to ensure the solution is sufficiently close to the slow manifold. A FSNN is trained on this dataset using the Adam optimizer from Optax. The INN consists of one outer layer, where the inner coupling flow layers consists of feedforward networks with one layer and a hidden dimension of 40. The feedforward neural networks on the RHS of the neural ODE system each consist of 50 layers and the bilinear form has a rank of 1. Considering each coefficient and its real and imaginary parts, the dimension of the learned model is  $\mathbb{R}^{30}$ , with  $N_x = 18$  and  $N_y = 12$ .

Table 1

Comparison of ground truth eigenvalues of the Jacobian of the fast equations with that of the trained model for the Grad Moment System problem.

Grad Eigenvalues					
g.t.	model	error	g.t.	model	error
-1	-0.9971	2.9e-03	$-\frac{2}{3}$	-0.6659	8.2e-04
-1	-0.9969	3.1e-03	$-\frac{2}{3}$	-0.6658	8.3e-04
-1	-0.9969	3.1e-03	$-\frac{2}{3}$	-0.6658	9.1e-04
-1	-0.9968	3.2e-03	$-\frac{2}{3}$	-0.6657	9.3e-04
-1	-0.9968	3.2e-03	$-\frac{2}{3}$	-0.6657	9.4e-04
-1	-0.9968	3.2e-03	$-\frac{2}{3}$	-0.6657	9.4e-04

Figure 6 shows comparisons of the trained model and reference solutions on the fast time scale and slow time scale. The results demonstrate that the model is accurate on both time scales. Table 1 shows a comparison of the eigenvalues of the trained model with the analytical eigenvalues. Great agreement is observed, which implies that the model was successful in mapping the slow manifold approximately to the true slow manifold.

It is critical to stress that the slow dynamics comparison in Figure 6 is done through integration on the slow manifold using (3.23). Specifically, the initial condition state vector  $z_0$  is first transformed into the fast-slow coordinates  $(x_0, y_0)$  and projected onto the learned slow manifold  $(x_0, 0)$  before integrating the slow variable  $x$  on the slow time scale only and then transforming back into original coordinates using  $h^{-1}$ . This approach is significantly more efficient than integrating the full system. The excellent accuracy of the predicted slow variable solution indicates a data-driven *closure* is learned through this procedure. The closure of (5.3) formally exists when  $\epsilon$  approaches 0. It is readily seen that the reduced system is a linearized Euler system.

**5.4. Multi-Scale Lorenz96 Equations.** In this section we consider the two-scale Lorenz96 equations, which was a model proposed in [47] as a test bed model for multi-scale behavior in atmospheric dynamics. The original system is formulated as

$$(5.7a) \quad \frac{d}{d\tau} X_k = -X_{k-1}(X_{k-2} - X_{k+1}) - X_k + F - (hc/b) \sum_{j=1}^J Y_{j,k},$$

$$(5.7b) \quad \frac{d}{d\tau} Y_{j,k} = -cbY_{j+1,k}(Y_{j+2,k} - Y_{j-1,k}) - cY_{j,k} + (hc/b)X_k,$$

for  $j = 1, \dots, J$  and  $k = 1, \dots, K$ , where the solutions satisfy periodicity ( $X_{k+K} = X_k$ ,  $Y_{j,k+K} = Y_{j,k}$ ,  $Y_{j+J,k} = Y_{j,k}$ ). Let  $c = b = 1/\epsilon$ ,  $h = 1$ ,  $Y = \epsilon y$ ,  $\tau = \epsilon t$ , and  $F = 0$ . The system becomes

$$(5.8a) \quad \frac{d}{dt} x_k = -\epsilon x_{k-1}(x_{k-2} - x_{k+1}) - \epsilon x_k - \epsilon^2 \sum_{j=1}^J y_{j,k},$$

$$(5.8b) \quad \frac{d}{dt} y_{j,k} = -y_{j+1,k}(y_{j+2,k} - y_{j-1,k}) - y_{j,k} + x_k.$$

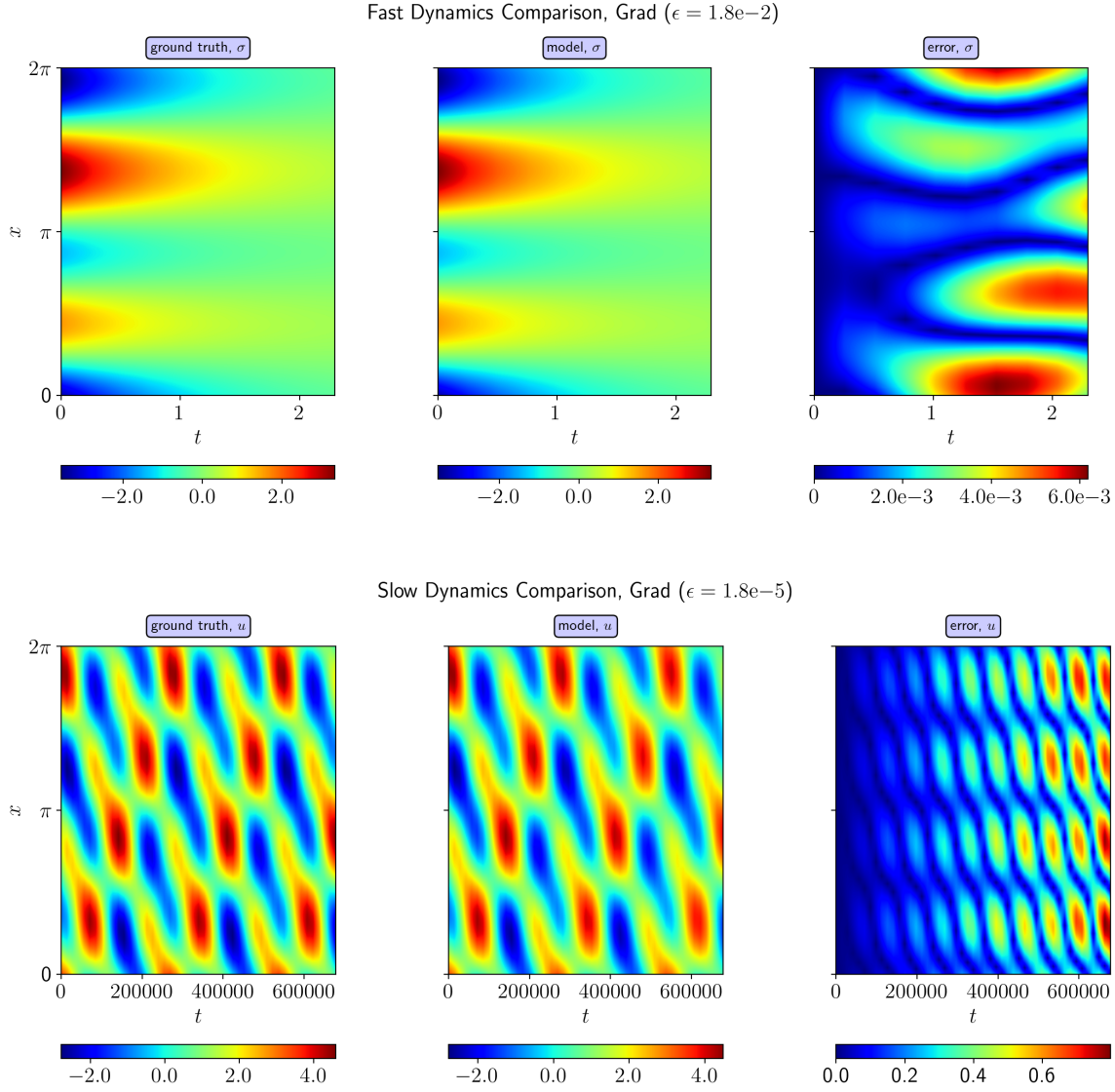


**Figure 6.** Comparison of fast scale (top) and slow scale (bottom) dynamics between the ground truth and trained model for the Grad moment system example.

Since the FSNN is limited to representing normally stable fast-slow systems, we explore the region of applicability where (5.8) is a normally fast-slow system. The normally stable region of Lorenz96 is identified by the following theorem.

**Theorem 5.1.** *The system of equations defined by (5.8) represent a normally stable fast-*

slow system when  $-\frac{1}{2} < x_k < \frac{8}{9}$ , for  $k = 1, \dots, K$ .

Using Definition 2.3, we need to show that the Jacobian of the right-hand-side of (5.8b) has eigenvalues strictly to the left of the imaginary axis. Consider the following nonlinear equation  $f(y; \chi) \in \mathbb{R}^J$  for  $y \in \mathbb{R}^J$  and  $\chi \in \mathbb{R}$ .

$$(5.9) \quad f(y; \chi) = -y_{j+1}(y_{j+2} - y_{j-1}) - y_j + \chi.$$

The Jacobian of this equation,  $D_y f$  is given by

$$(5.10) \quad (D_y f)_{jk} = \frac{\partial f_j}{\partial y_k} = -\delta_{jk} - \delta_{j+1,k}(y_{j+2} - y_{j-1}) - y_{j+1}(\delta_{j+2,k} - \delta_{j-1,k}),$$

where  $\delta_{jk}$  represents the Kronecker delta. We are interested in the eigenvalues of  $D_y$  when  $f(y; \chi) = 0$ . Note that one solution to  $f(y; \chi) = 0$  is given by  $y_j = \chi$  for  $j = 1, \dots, J$ . At this fixed point, the Jacobian becomes

$$(5.11) \quad (D_y f)_{jk}|_{y=\chi} = -\delta_{jk} - \chi(\delta_{j+2,k} - \delta_{j-1,k})$$

This represents a circulant matrix, of which the eigenvalues are given by

$$(5.12) \quad \lambda_j = -1 - \chi(e^{ij4\pi/J} - e^{-ij2\pi/J}), \quad j = 0, 1, \dots, J-1.$$

Note that

$$(5.13) \quad \text{Re}(\lambda_j) = -1 - \chi(\cos(4\xi_j) - \cos(2\xi_j)),$$

where  $\xi_j = 4\pi j/J$ . We are interested in the region for  $\chi$  where  $\text{Re}(\lambda_j) < 0$  for all  $j$ . As  $J \rightarrow \infty$ , we have the bound  $-\frac{9}{8} \leq \cos(4\xi_j) - \cos(2\xi_j) \leq 2$ . This implies that the region is given by  $-\frac{1}{2} < x < \frac{8}{9}$ . For a finite  $J$ , the bounds of  $\cos(4\xi_j) - \cos(2\xi_j)$  are determined by the resolution of  $\xi_j$ , which is a discrete function of  $j$ . This affords us to take a slightly wider region of  $x$  where  $\text{Re}(\lambda_j) < 0$  for all  $j$ . For example, when  $J = 4$ ,  $-\frac{1}{2} < x < 1$ .

Homotopy continuation can be used on the polynomial system of equations defined by  $f$  to reveal a high-order polynomial containing all possible roots. Maple was used to evaluate all the roots for multiple values of  $\chi$  and for  $J = 4, 5, 6$ . Within the region  $\chi \in (-\frac{1}{2}, \frac{8}{9})$ , the only real-valued solution is given by  $y_j = \chi$  for  $j = 1, \dots, J$ . We conjecture that there is only a single real-valued solution to (5.9) when  $\chi \in (-\frac{1}{2}, \frac{8}{9})$  for  $J > 6$ .

We have shown that the multi-scale Lorenz96 equations are normally-stable for a restricted range of  $x_k$ . However, for any  $x_k, y_{j,l}, \epsilon > 0$ , the system is energy stable, which implies that, for any initial condition, the energy will decay in time and the dynamics will eventually be able to be described by a normally fast-slow system for some time  $t > 0$ .

**Theorem 5.2.** *The equations defined by (5.8) are energy-stable for  $\epsilon > 0$ .*

Consider again the original system. We multiply the equations by  $x_k$  and  $y_{j,k}$ , respectively. Let  $(\cdot)' = \frac{d}{dt}(\cdot)$ , then

$$(5.14a) \quad x_k x'_k = -\epsilon x_k x_{k-1}(x_{k-2} - x_{k+1}) - \epsilon x_k^2 - \epsilon^2 \sum_{j=1}^J x_k y_{j,k}$$

$$(5.14b) \quad y_{j,k} y'_{j,k} = -y_{j,k} y_{j+1,k}(y_{j+2,k} - y_{j-1,k}) - y_{j,k}^2 + x_k y_{j,k}.$$

We collect the terms and take the sum over the discrete variables.

$$\begin{aligned} \frac{1}{2} \sum_{k=1}^K (x_k^2)' &= -\epsilon \sum_{k=1}^K x_k x_{k-1} x_{k-2} + \epsilon \sum_{k=1}^K x_{k+1} x_k x_{k-1} - \epsilon \sum_{k=1}^K x_k^2 - \epsilon^2 \sum_{k=1}^K \sum_{j=1}^J x_k y_{j,k} \\ \frac{1}{2} \sum_{j=1}^J (y_{j,k}^2)' &= -\sum_{j=1}^J y_{j,k} y_{j+1,k} y_{j+2,k} + \sum_{j=1}^J y_{j-1,k} y_{j,k} y_{j+1,k} - \sum_{j=1}^J y_{j,k}^2 + \sum_{j=1}^J x_k y_{j,k} \end{aligned}$$

Due to periodicity, the cubic terms evaluate to zero. The remaining terms give us the following energy estimate.

$$(5.15) \quad \frac{1}{2} \sum_{k=1}^K (x_k^2)' + \frac{1}{2} \epsilon^2 \sum_{k=1}^K \sum_{j=1}^J (y_{j,k}^2)' = -\epsilon \sum_{k=1}^K x_k^2 - \epsilon^2 \sum_{k=1}^K \sum_{j=1}^J y_{j,k}^2 < 0$$

We train a FSNN to learn the multi-scale Lorenz96 equations from data. The trajectory dataset,  $\mathcal{D}$ , consists of  $10^4$  fast-scale trajectories, corresponding to initial conditions for  $x_k$  randomly generated uniformly in  $[-\frac{1}{2}, 1]$  and  $y_{j,k}$  randomly generated from a normal distribution,  $\epsilon$  randomly generated log-uniformly in  $[10^{-5}, 10^{-2}]$ , and integrated forward 10 timesteps using an adaptive RK45 solver with error tolerance  $10^{-8}$ . The manifold dataset,  $\mathcal{M}$  consists of  $10^4$  examples of data pairs  $((x_k, y_{j,k}), \epsilon = 0)$  on the graph  $y_{j,k} = x_k$ , where  $x_k$  is randomly generated uniformly in  $[-\frac{1}{2}, 1]$ .

A FSNN is trained on this dataset using the Adam optimizer from Optax. The INN consists of one outer layer, where the inner coupling flow layers consists of feedforward networks with one layer and a hidden dimension of 40. The feedforward neural networks on the RHS of the neural ODE system each consist of 40 layers and the bilinear form has a rank of 4.

Figure 7 shows a comparison of the trained model and the reference solution for an example initial condition with  $\epsilon = 1.1 \cdot 10^{-3}$ . The model shows quantitative agreement to the reference solution. Figure 8 shows a comparison of the eigenvalues of the trained model with the analytical eigenvalues. Agreement is observed, implying that the model was successful in mapping the slow manifold approximately to the true slow manifold. In this example, the time interval of all the training data is much shorter than  $t = 3$ . Nevertheless, the prediction can be done up to  $T = 3000$  or longer with excellent accuracy.

**5.5. Abraham-Lorentz Equations.** In this section, we consider the Abraham-Lorentz equations [10], which model the radiation reaction in the case of a single electron with charge  $e$  and mass  $m$  moving through a static external magnetic field  $\mathbf{B}(\mathbf{x}) \in \mathbb{R}^3$ . The equations are given by

$$(5.16a) \quad \frac{2}{3} \frac{e^2}{c^3} \frac{d\mathbf{a}}{d\tau} = m\mathbf{a} - \frac{e}{c} \mathbf{v} \times \mathbf{B}(\mathbf{x}),$$

$$(5.16b) \quad \frac{d\mathbf{v}}{d\tau} = \mathbf{a},$$

$$(5.16c) \quad \frac{d\mathbf{x}}{d\tau} = \mathbf{v},$$



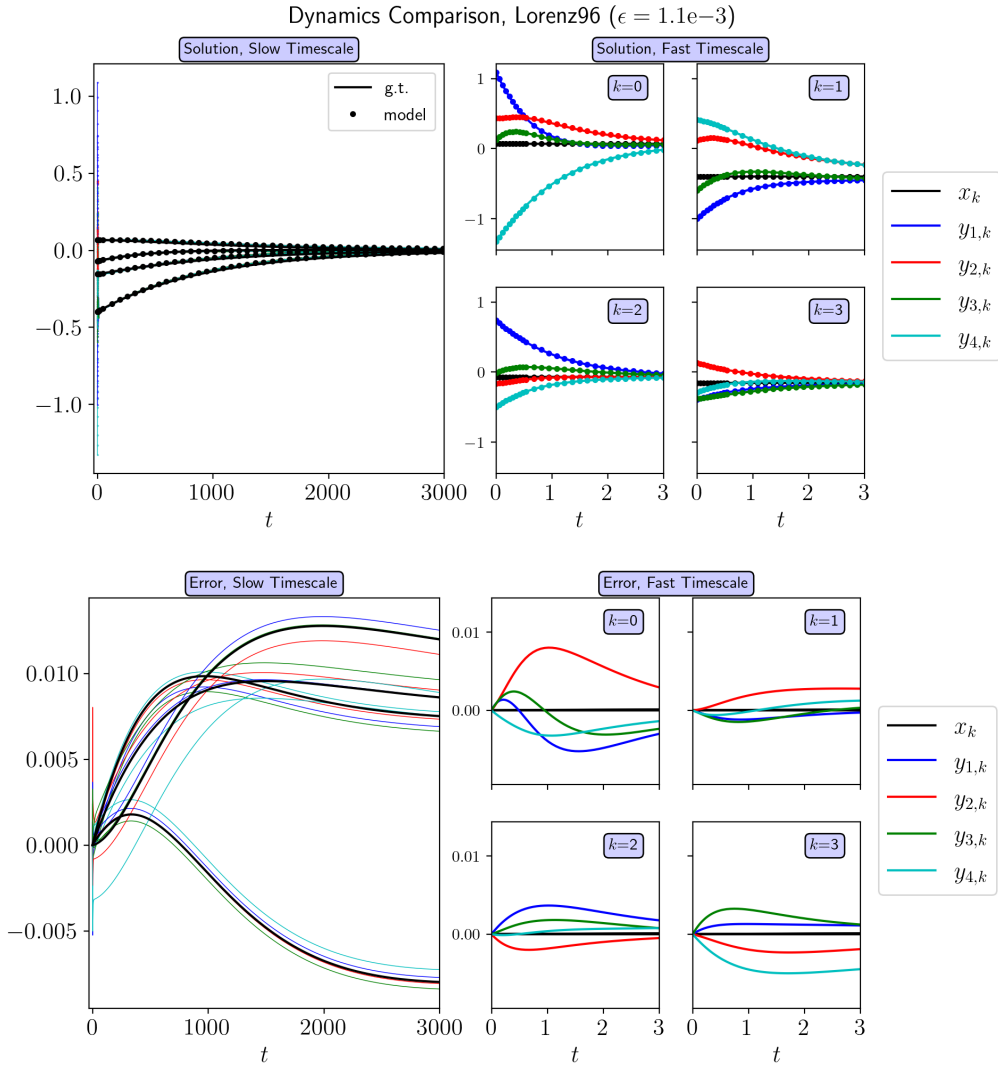


**Figure 7.** The top five plots are trajectory plots comparing the reference solution computed using RK45 (bold curves) and that of the trained model (dotted markers) for an initial condition with  $\epsilon = 1.1 \cdot 10^{-3}$  for the multi-scale Lorenz96 example described by the dynamics in (5.8). The bottom five plots show the corresponding errors as a function of time. The plots in the left column show the solution and error on the slow time scale ( $t \in [0, 3000]$ ) while the plots in the right column zoom in on the fast time scale ( $t \in [0, 3]$ ).

where  $\mathbf{x}(\tau), \mathbf{v}(\tau), \mathbf{a}(\tau) \in \mathbb{R}^3$  are the position, velocity, and acceleration, respectively, and  $c$  is the speed of light. We rescale these equations following the approach in [10]. Time is scaled by the observer time scale  $T$  as  $\tau = T\bar{\tau}$ , space by the observer length scale  $\mathbf{x} = L\bar{\mathbf{x}}$ , velocity as  $\mathbf{v} = (L/T)\bar{\mathbf{v}}$ , the magnetic field as  $\mathbf{B}(\mathbf{x}) = B_0\bar{\mathbf{B}}(\bar{\mathbf{x}})$ , and acceleration as  $a = (L/T)(|e|B_0)(mc)^{-1}\bar{a}$ . We reformulate the rescaled Abraham-Lorentz equations in terms of

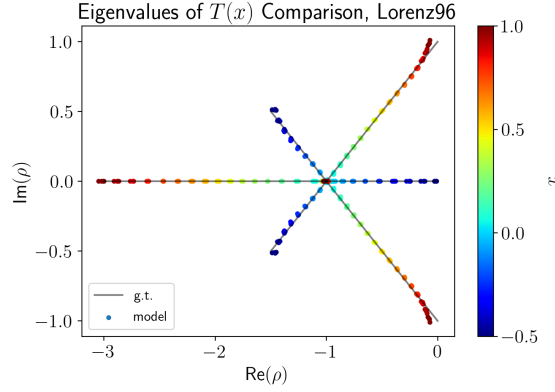


**Figure 8.** Comparison of the true eigenvalues (bold lines) with those learned from the trained model (dots) for the multi-scale Lorenz96 example described by the dynamics in (5.8)

the nondimensional variables and drop the overline for notational convenience.

$$(5.17a) \quad \left(\frac{r_0}{cT}\right) \frac{2}{3} \frac{d\mathbf{a}}{d\tau} = \mathbf{a} - \zeta \mathbf{v} \times \mathbf{B}(\mathbf{x}),$$

$$(5.17b) \quad \frac{d\mathbf{v}}{d\tau} = (\omega_c T) \mathbf{a},$$

$$(5.17c) \quad \frac{d\mathbf{x}}{d\tau} = \mathbf{v},$$

where we have introduced the cyclotron frequency  $\omega_c = |e|B_0/(mc)$ , the classical electron radius  $r_0 = e^2/(mc)^2$ , and the sign of the charge  $\zeta \in \{-1, +1\}$ , where  $\zeta = -1$  corresponds to electrons and  $\zeta = +1$  to positrons. The dimensionless parameters

$$(5.18) \quad \gamma_R = \frac{r_0}{cT}, \quad \gamma_B = \frac{1}{\omega_c T},$$

represent the ratio of the electron size to the distance light travels during a time interval  $T$ , and ratio of the cyclotron period to  $T$ , respectively. The system can be transformed into a two-scale fast-slow system with the choice  $\gamma_B = 1$  and  $\gamma_R = \epsilon \ll 1$ . We scale time through the transformation  $\tau = \frac{2}{3}\epsilon t$  to reveal a normally-unstable fast-slow system given by

$$(5.19a) \quad \frac{d\mathbf{a}}{dt} = \mathbf{a} - \zeta \mathbf{v} \times \mathbf{B}(\mathbf{x}),$$

$$(5.19b) \quad \frac{d\mathbf{v}}{dt} = \epsilon \frac{2}{3} \mathbf{a},$$

$$(5.19c) \quad \frac{d\mathbf{x}}{dt} = \epsilon \frac{2}{3} \mathbf{v},$$

We will refer to (5.19) as the *forward-time Abraham-Lorentz system*. A normally-stable fast-slow system can be obtained by reversing time using  $t_- = -t$ ,

$$(5.20a) \quad \frac{d\mathbf{a}}{dt_-} = -\mathbf{a} + \zeta \mathbf{v} \times \mathbf{B}(\mathbf{x}),$$

$$(5.20b) \quad \frac{d\mathbf{v}}{dt_-} = -\epsilon \frac{2}{3} \mathbf{a},$$

$$(5.20c) \quad \frac{d\mathbf{x}}{dt_-} = -\epsilon \frac{2}{3} \mathbf{v}.$$

We refer to (5.20) as the *reverse-time Abraham-Lorentz system*. In both systems,  $\mathbf{a}$  is the fast variable and  $\mathbf{v}, \mathbf{x}$  are the slow variables. In reverse time, the acceleration,  $\mathbf{a}$  will be attracted to the slow manifold, given by

$$(5.21) \quad \mathbf{a}^*(\mathbf{x}, \mathbf{v}) = \zeta \mathbf{v} \times \mathbf{B}(\mathbf{x}) + \epsilon \frac{3}{2} \mathbf{v} \times \mathbf{B}(\mathbf{x}) \times \mathbf{B}(\mathbf{x}) + \mathcal{O}(\epsilon^2).$$

Though the reverse-time system is stable on the fast time scale, the system exhibits an instability tangential to the slow manifold for which solutions blow up on the slow time scale. This is a more challenging test than the previous ones.

It is of interest to obtain forward-time trajectories of electrons along the slow manifold. A standard numerical integration of (5.19) will result in unstable trajectories on the fast time scale since any numerical error will push trajectories off of the slow-manifold, resulting in exponential growth of the acceleration. We instead apply FSNNs to learn the Fenichel normal form of the system in *reverse time*. We then obtain forward-time trajectories along the learned slow manifold by performing an integration of the slow variables along  $y = 0$  using (3.23). This test is therefore a more practical application of a data-driven closure.

We train a FSNN to learn the Abraham-Lorentz equations from data. The trajectory dataset,  $\mathcal{D}$ , consists of  $10^4$  trajectories, corresponding to initial conditions randomly generated in the region,  $\mathcal{R}$ , specified by

$$\mathcal{R} = \{\mathbf{x}, \mathbf{v}, \mathbf{a} : 2 \leq r \leq 4, \quad |z| \leq 1, \quad \|\mathbf{v}\| \leq 1, \quad \|\mathbf{a} - \mathbf{a}^*(\mathbf{x}, \mathbf{v})\| \leq 1\},$$

where  $r = \sqrt{x_1^2 + x_2^2}$  and  $z = x_3$ .  $\epsilon$  is randomly generated log-uniformly in the range  $[10^{-5}, 10^{-2}]$ . The trajectories are integrated in reverse time using equations (5.20) using an adaptive RK45 solver set to an error tolerance of  $10^{-8}$ . The first 40 time steps batched in sequences of length 10 are used as fast-scale training data. These trajectories are also interpolated over a slower time scale with  $\Delta t = 0.025/\epsilon$  and  $10^4$  sequences of length 10 are chosen at random for slow-scale training data. The manifold dataset,  $\mathcal{M}$  consists of  $10^4$  examples of data pairs  $((\mathbf{x}, \mathbf{v}, \mathbf{a}), \epsilon = 0)$  on the graph  $\mathbf{a} = \mathbf{v} \times \mathbf{B}(\mathbf{x})$ , where  $\mathbf{x}, \mathbf{v}$  are randomly generated in the region  $\mathcal{R}$ .

The magnetic field is chosen to be  $\mathbf{B} = B_r \mathbf{e}_r + B_\phi \mathbf{e}_\phi + B_z \mathbf{e}_z$ , where  $\mathbf{e}_r, \mathbf{e}_\phi, \mathbf{e}_z$  represent basis vectors for cylindrical coordinates, and

$$(5.22) \quad B_r = -\frac{z}{q(r, z)r} B_0, \quad B_\phi = \frac{R_0}{r} B_0, \quad B_z = \frac{(r - R_0)}{q(r, z)r} B_0,$$

where  $q(r, z) = q_0 + q_2((r - R_0)(r - R_0) + z^2)/a^2$  and  $q_0 = 1.2$ ,  $q_2 = 2.8$ ,  $a = 1.5$ ,  $R_0 = 3.0$ ,  $Z_0 = 3.0$ , and  $B_0 = 1.0$ . This field is an idealized equilibrium of a tokamak, where the field is physical inside a torus with major radius of  $R_0$  and minor radius of  $a$ . Here  $q$  is called a safety factor [45] and the poloidal magnetic flux function is  $\psi = \frac{B_0 a^2}{2q_2} \ln(q)$ . Under this definition, the given field can be rewritten as

$$(5.23) \quad \mathbf{B} = \frac{1}{R} \nabla \psi \times \mathbf{e}_\phi + \frac{F_0}{R} \mathbf{e}_\phi.$$

where the poloidal field is a constant of  $F_0 = R_0 B_0$ . This test thus models a charged particle moving through a tokamak with radiation reaction.

A FSNN is trained on this dataset using the Adam optimizer from Optax. The INN consists of one outer layer, where the inner coupling flow layers consists of feedforward networks with one layer and a hidden dimension of 50. The function  $g$  on the right-hand-side of the neural ODE uses a single-layer feedforward neural network with hidden dimension 100 and is added to a bilinear form network with rank 1. The remaining feedforward neural networks on the right-hand-side of the neural ODE system each consist of 50 layers and the bilinear form has a rank of 4.

Figure 9 shows comparisons of the solutions in  $r$ – $z$  space between the trained network and trajectories computed using RK45 on the reverse-time system. Using the reverse-time trajectories, endpoints were supplied as initial conditions to the trained network to predict forward in time. For both the reverse-time predictions (red arrows) and forward-time predictions (green arrows), the the trained model agrees well with the solution computed numerically. The corresponding  $L_2$  errors are shown for position, velocity, and acceleration in Figure 10, demonstrating that errors are low when integrating on the slow time scale.

**Table 2**

*Comparison of true eigenvalues to the eigenvalues of the trained model for the Abraham-Lorentz problem.*

Reverse-Time Abraham-Lorentz System Eigenvalues		
g.t.	model	error
-1	-0.99962	3.8e-04
-1	-0.99958	4.2e-04
-1	-0.99958	4.2e-04

Table 2 shows the comparison of the true eigenvalues of the linear part of the fast dynamics of the reverse-time system. The eigenvalues were recovered with a great deal of accuracy, demonstrating that the fast-scale dynamics are learned accurately.

Figure 11 shows comparisons of orbits between the trained model and orbits obtained when integrating the system by substituting the first two terms of the asymptotic expansion in (5.21). Note again that when integrating along the slow manifold, only the slow variable is evolved using the transformation  $h$  and the closure  $y = 0$ . The trained model is able to qualitatively capture the gyro-motion behavior while also accurately capturing the guiding center dynamics over the slow time scale. Despite training using a limited number of trajectories over a relatively short time frame (2 or less gyration periods) due to the slow time scale instability of the reverse-time system, the trained network is highly capable of predicting long-time

dynamics in forward-time for many more gyration cycles. We remind the reader that standard numerical methods cannot integrate the forward-time Abraham-Lorentz system along the slow manifold without experiencing an exponential growth instability. Direct integration of the asymptotic expansion removes the instability, but introduces an error dependent on  $\epsilon$  due to the asymptotic approximation. This result highlights the unique capability of the proposed network.

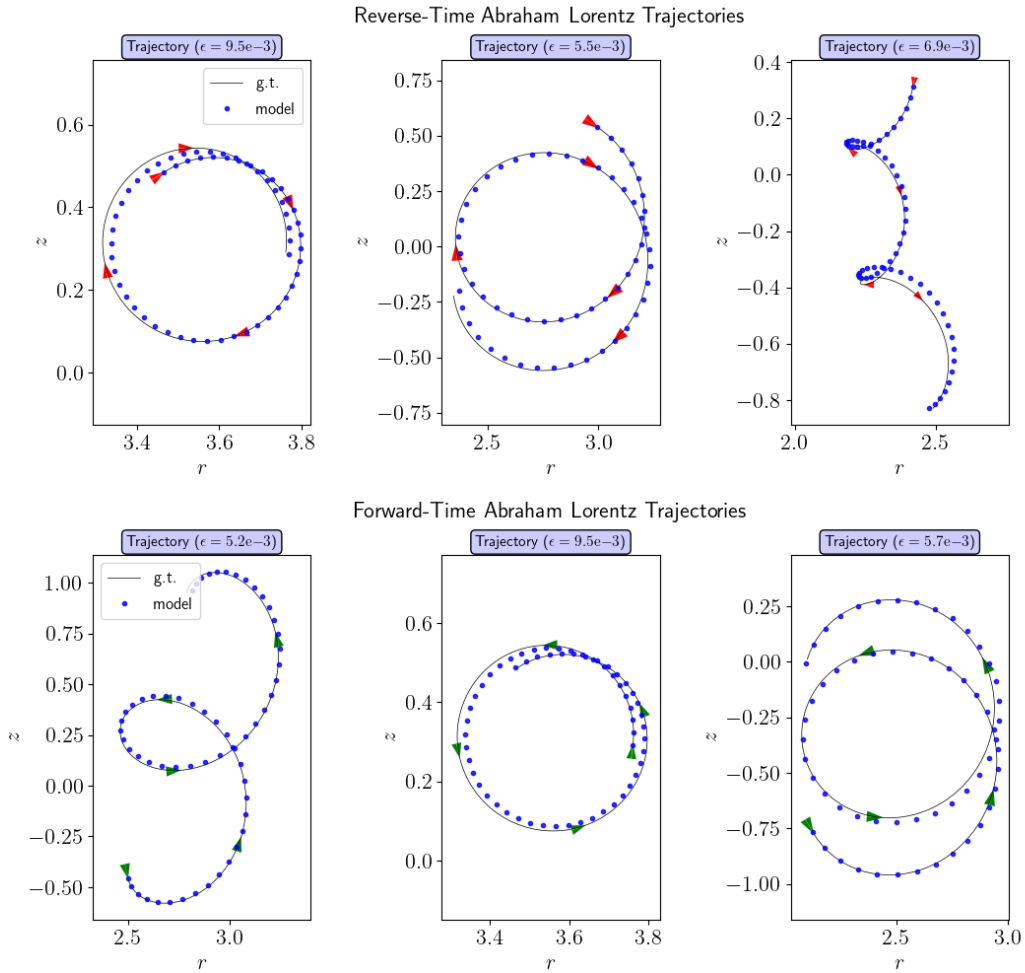


**Figure 9.** Displayed are the trajectories for three values of  $\epsilon$  evolved backwards in time along the slow manifold (top three plots, red arrows) and three values of  $\epsilon$  evolved forwards in time along the slow manifold (bottom three plots, green arrows). The solid lines represent the ground truth trajectories and the dotted lines represent the model.

**6. Conclusions.** In this paper, we introduced the fast-slow neural network (FSNN), which is a data-driven approach suitable for learning singularly perturbed dynamical systems where the fast-scale dynamics are dissipative. Our method enforces the existence of a trainable,

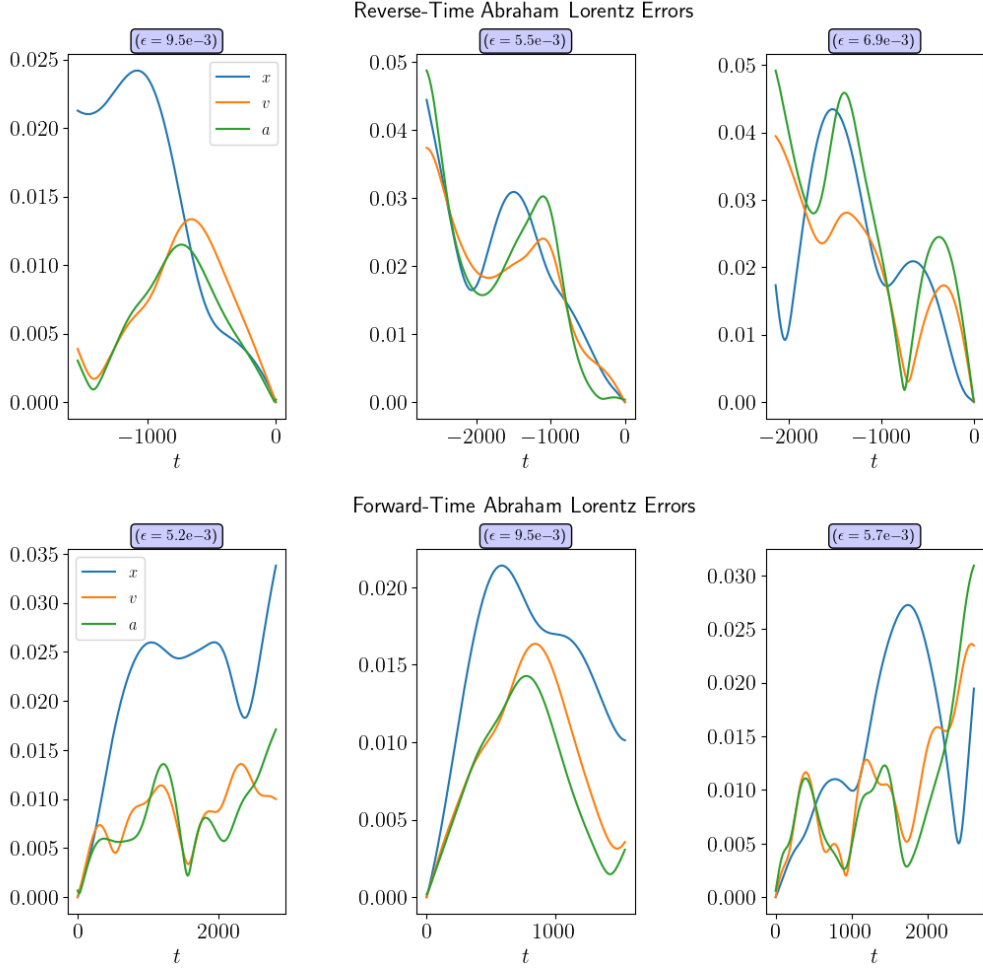


**Figure 10.** Error trajectories for the reverse time (top three plots) and forward time simulations are displayed. For each simulation, the  $L_2$  norm of position, velocity and acceleration are plotted.

attracting invariant slow manifold as a hard constraint. Invertible neural networks and neural ODEs are key components of the FSNN. We introduce bi-Lipschitz affine transformation (bLAT) layers for enforcing regularity of the invertible neural network. We also develop a negative Schur form network which parameterizes matrices with eigenvalues to the left of the imaginary axis. This in addition to the use of an additive L-stable diagonally-implicit Runge Kutta scheme for integration are key pieces in ensuring that the fast-scale dynamics are stable. The Schur form network also enables the use of back-substitution to efficiently handle the implicit solve. Analytical representation of the slow manifold enables efficient integration on the slow time scale. We demonstrate the FSNN on many examples that exhibit two timescales, including the Grad moment system from hydrodynamics, two-scale Lorentz96 equations for modeling atmospheric dynamics, and Abraham-Lorentz dynamics modeling radiation reaction

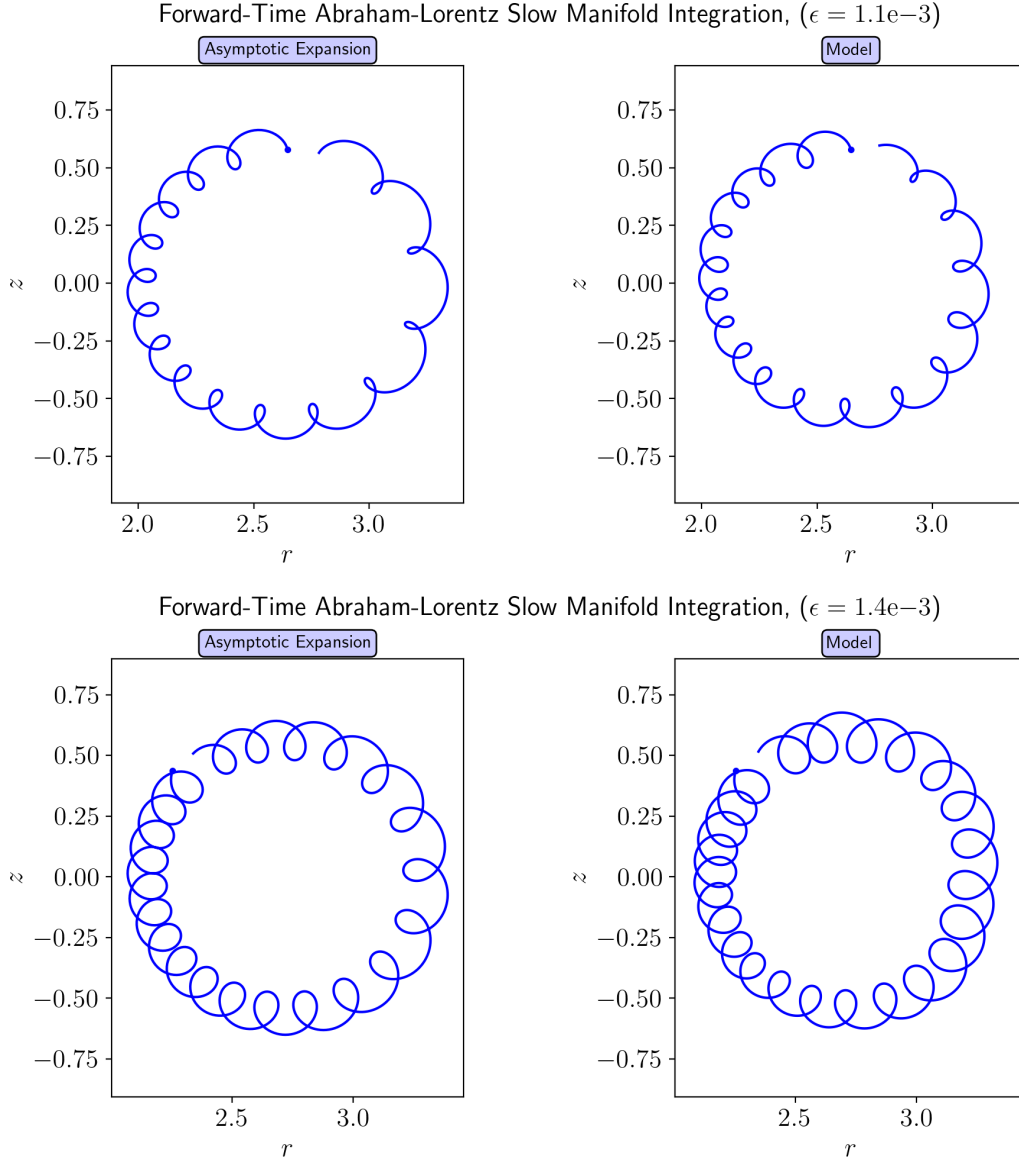


**Figure 11.** Comparison of orbits of the forward-time Abraham-Lorentz system (5.19) along the slow manifold for the first two terms of the asymptotic expansion in (5.21) (left) and the trained model (right) for two different initial conditions and choices of  $\epsilon$ .

of electrons in a magnetic field.

The proposed network can be used to discover a full-order model with long-term accuracy near a slow manifold when only short duration trajectories are available. The proposed network is also applicable to discover a reduced-order model as a unique closure discovery procedure.



**Acknowledgment.** This research used resources provided by the Los Alamos National Laboratory Institutional Computing Program, which is supported by the U.S. Department of Energy National Nuclear Security Administration under Contract No. 89233218CNA000001, and the National Energy Research Scientific Computing Center (NERSC), a U.S. Department of Energy Office of Science User Facility located at Lawrence Berkeley National Laboratory, operated under Contract No. DE-AC02-05CH11231 using NERSC award ASCR-ERCAP0023112.

## REFERENCES

- [1] L. ARDIZZONE, J. KRUSE, S. WIRKERT, D. RAHNER, E. W. PELLEGRINI, R. S. KLESSSEN, L. MAIERHEIN, C. ROTHER, AND U. KÖTHE, *Analyzing inverse problems with invertible neural networks*, arXiv preprint arXiv:1808.04730, (2018).
- [2] Z.-Z. BAI AND J.-Y. PAN, *Matrix Analysis and Computations*, 01 2021.
- [3] Y. BAR-SINAI, S. HOYER, J. HICKEY, AND M. P. BRENNER, *Learning data-driven discretizations for partial differential equations*, Proceedings of the National Academy of Sciences, 116 (2019), pp. 15344–15349.
- [4] P. BENNER, S. GUGERCIN, AND K. WILLCOX, *A survey of projection-based model reduction methods for parametric dynamical systems*, SIAM Review, 57 (2015), pp. 483–531.
- [5] G. BERKOOZ, P. HOLMES, AND J. L. LUMLEY, *The proper orthogonal decomposition in the analysis of turbulent flows*, Annual review of fluid mechanics, 25 (1993), pp. 539–575.
- [6] J. F. BLINN, *Consider the lowly 2 x 2 matrix*, IEEE Computer Graphics and Applications, 16 (1996), pp. 82–88.
- [7] J. BRADBURY, R. FROSTIG, P. HAWKINS, M. J. JOHNSON, C. LEARY, D. MACLAURIN, G. NECULA, A. PASZKE, J. VANDERPLAS, S. WANDERMAN-MILNE, AND Q. ZHANG, *JAX: composable transformations of Python+NumPy programs*, 2018.
- [8] S. BRAGINSKII, *Transport processes in a plasma*, Reviews of plasma physics, 1 (1965), p. 205.
- [9] J. BURBY, Q. TANG, AND R. MAULIK, *Fast neural Poincaré maps for toroidal magnetic fields*, Plasma Physics and Controlled Fusion, 63 (2020).
- [10] J. W. BURBY AND T. KLOTZ, *Slow manifold reduction for plasma science*, Commun. Nonlinear Sci. Numer. Simul., 89 (2020), p. 105289.
- [11] R. T. CHEN, Y. RUBANOVA, J. BETTENCOURT, AND D. K. DUVENAUD, *Neural ordinary differential equations*, Advances in neural information processing systems, 31 (2018).
- [12] A. J. CHORIN AND F. LU, *Discrete approach to stochastic parametrization and dimension reduction in nonlinear dynamics*, Proceedings of the National Academy of Sciences, 112 (2015), pp. 9804–9809.
- [13] R. R. COIFMAN AND S. LAFON, *Diffusion maps*, Applied and computational harmonic analysis, 21 (2006), pp. 5–30.
- [14] T. CUI, T. BERTALAN, G. J. PAPPAS, M. MORARI, I. G. KEVREKIDIS, AND M. FAZLYAB, *Certified invertibility in neural networks via mixed-integer programming*, 2023, <https://arxiv.org/abs/2301.11783>.
- [15] G. V. CYBENKO, *Approximation by superpositions of a sigmoidal function*, Mathematics of Control, Signals and Systems, 2 (1989), pp. 303–314.
- [16] C. E. P. DE JESÚS AND M. D. GRAHAM, *Data-driven low-dimensional dynamic model of kolmogorov flow*, Phys. Rev. Fluids, 8 (2023), p. 044402.
- [17] DEEPMIND, I. BABUSCHKIN, K. BAUMLI, A. BELL, S. BHUPATIRAJU, J. BRUCE, P. BUCHLOVSKY, D. BUDDEN, T. CAI, A. CLARK, I. DANIHELKA, A. DEDIEU, C. FANTACCI, J. GODWIN, C. JONES, R. HEMSLEY, T. HENNIGAN, M. HESSEL, S. HOU, S. KAPUROWSKI, T. KECK, I. KEMAEV, M. KING, M. KUNESCH, L. MARTENS, H. MERZIC, V. MIKULIK, T. NORMAN, G. PAPAMAKARIOS, J. QUAN, R. RING, F. RUIZ, A. SANCHEZ, L. SARTRAN, R. SCHNEIDER, E. SEZENER, S. SPENCER, S. SRINIVASAN, M. STANOJEVIĆ, W. STOKOWIEC, L. WANG, G. ZHOU, AND F. VIOLA, *The DeepMind JAX Ecosystem*, 2020, <http://github.com/google-deeppmind>.

- [18] L. DINH, J. SOHL-DICKSTEIN, AND S. BENGIO, *Density estimation using real NVP*, arXiv preprint arXiv:1605.08803, (2016).
- [19] G.-R. DUAN AND R. J. PATTON, *A note on hurwitz stability of matrices*, Automatica, 34 (1998), pp. 509–511.
- [20] V. DURUISSEAUX, J. W. BURBY, AND Q. TANG, *Approximation of nearly-periodic symplectic maps via structure-preserving neural networks*, Scientific Reports, 13 (2023), p. 8351.
- [21] N. FENICHEL, *Geometric singular perturbation theory for ordinary differential equations*, Journal of Differential Equations, 31 (1979), pp. 53–98.
- [22] C. FOIAS, M. JOLLY, I. KEVREKIDIS, G. SELL, AND E. TITI, *On the computation of inertial manifolds*, Physics Letters A, 131 (1988), pp. 433–436.
- [23] C. FOIAS, G. SELL, AND E. TITI, *Exponential tracking and approximation of inertial manifolds for dissipative nonlinear equations*, Journal of Dynamics and Differential Equations, 1 (1989), pp. 199–244.
- [24] C. FOIAS, G. R. SELL, AND R. TEMAM, *Inertial manifolds for nonlinear evolutionary equations*, Journal of differential equations, 73 (1988), pp. 309–353.
- [25] N. GICQUEL, J. ANDERSON, AND I. KEVREKIDIS, *Noninvertibility and resonance in discrete-time neural networks for time-series processing*, Physics Letters A, 238 (1998), pp. 8–18.
- [26] A. GORBAN AND I. KARLIN, *Hilbert’s 6th problem: Exact and approximate hydrodynamic manifolds for kinetic equations*, Bulletin of the American Mathematical Society, 51 (2013), pp. 186–246.
- [27] H. GRAD, *On the kinetic theory of rarefied gases*, Communications on Pure and Applied Mathematics, 2 (1949), pp. 331–407.
- [28] J.-L. GUERMOND AND S. PRUDHOMME, *A fully discrete nonlinear galerkin method for the 3d navier-stokes equations*, Numerical Methods for Partial Differential Equations, 24 (2008), pp. 759 – 775.
- [29] G. W. HAMMETT AND F. W. PERKINS, *Fluid moment models for Landau damping with application to the ion-temperature-gradient instability*, Physical review letters, 64 (1990), p. 3019.
- [30] R. A. HORN AND C. R. JOHNSON, *Matrix Analysis*, Cambridge University Press, 1985.
- [31] F. JAUBERTEAU, C. ROSIER, AND R. TEMAM, *A nonlinear galerkin method for the navier-stokes equations*, Computer Methods in Applied Mechanics and Engineering, 80 (1990), pp. 245–260.
- [32] P. JIN, Z. ZHANG, A. ZHU, Y. TANG, AND G. E. KARNIADAKIS, *SympNets: Intrinsic structure-preserving symplectic networks for identifying hamiltonian systems*, Neural Networks, 132 (2020), pp. 166–179.
- [33] M. S. JOLLY, *Explicit construction of an inertial manifold for a reaction diffusion equation*, Journal of Differential Equations, 78 (1989), pp. 220–261.
- [34] M. S. JOLLY, I. KEVREKIDIS, AND E. S. TITI, *Approximate inertial manifolds for the Kuramoto-Sivashinsky equation: analysis and computations*, Physica D: Nonlinear Phenomena, 44 (1990), pp. 38–60.
- [35] C. JONES, *Geometric singular perturbation theory*, 1995.
- [36] E. D. KORONAKI, N. EVANGELOU, C. P. MARTIN-LINARES, E. S. TITI, AND I. G. KEVREKIDIS, *Nonlinear dimensionality reduction then and now: AIMS for dissipative PDEs in the ML era*, 2023, <https://arxiv.org/abs/2310.15816>.
- [37] M. A. KRAMER, *Nonlinear principal component analysis using autoassociative neural networks*, AIChE Journal, 37 (1991), pp. 233–243.
- [38] K. KRISCHER, R. RICO-MARTÍNEZ, I. G. KEVREKIDIS, H. H. ROTERMUND, G. ERTL, AND J. L. HUDSON, *Model identification of a spatiotemporally varying catalytic reaction*, AIChE Journal, 39 (1993), pp. 89–98.
- [39] K. LEE AND K. T. CARLBERG, *Model reduction of dynamical systems on nonlinear manifolds using deep convolutional autoencoders*, Journal of Computational Physics, 404 (2020), p. 108973.
- [40] M. LEZCANO-CASADO, *Trivializations for gradient-based optimization on manifolds*, in Advances in Neural Information Processing Systems, NeurIPS, 2019, pp. 9154–9164.
- [41] A. J. LINOT, J. W. BURBY, Q. TANG, P. BALAPRAKASH, M. D. GRAHAM, AND R. MAULIK, *Stabilized neural ordinary differential equations for long-time forecasting of dynamical systems*, Journal of Computational Physics, 474 (2023), p. 111838.
- [42] A. J. LINOT AND M. D. GRAHAM, *Deep learning to discover and predict dynamics on an inertial manifold*, Phys. Rev. E, 101 (2020), p. 062209.
- [43] A. J. LINOT AND M. D. GRAHAM, *Data-driven reduced-order modeling of spatiotemporal chaos with*

- neural ordinary differential equations, *Chaos: An Interdisciplinary Journal of Nonlinear Science*, 32 (2022), p. 073110.
- [44] A. J. LINOT, K. ZENG, AND M. D. GRAHAM, *Turbulence control in plane couette flow using low-dimensional neural ode-based models and deep reinforcement learning*, *International Journal of Heat and Fluid Flow*, 101 (2023), p. 109139.
  - [45] S. LIU, Q. TANG, AND X.-Z. TANG, *A parallel cut-cell algorithm for the free-boundary Grad-Shafranov problem*, *SIAM Journal on Scientific Computing*, 43 (2021), pp. B1198–B1225.
  - [46] Y. LIU, J. N. KUTZ, AND S. L. BRUNTON, *Hierarchical deep learning of multiscale differential equation time-steppers*, *Philosophical Transactions of the Royal Society A*, 380 (2022), p. 20210200.
  - [47] E. LORENZ, *Predictability: a problem partly solved*, *Seminar on Predictability*, 4-8 September 1995, 1 (1995), pp. 1–18.
  - [48] F. LU, K. K. LIN, AND A. J. CHORIN, *Data-based stochastic model reduction for the kuramoto-sivashinsky equation*, *Physica D: Nonlinear Phenomena*, 340 (2017), pp. 46–57.
  - [49] L. PARESCHI AND G. RUSSO, *Implicit-explicit Runge-Kutta schemes and applications to hyperbolic systems with relaxation*, *Journal of Scientific Computing*, 25 (2005), pp. 129–155.
  - [50] R. RICO-MARTÍNEZ, I. KEVREKIDIS, AND K. KRISCHER, *Nonlinear system identification using neural networks: dynamics and instabilities*, *Neural networks for chemical engineers*, (1995), pp. 409–442.
  - [51] R. RICO-MARTÍNEZ, K. KRISCHER, I. G. KEVREKIDIS, M. C. KUBE, AND J. L. HUDSON, *Discrete- vs. continuous-time nonlinear signal processing of Cu electrodisolution data*, *Chemical Engineering Communications*, 118 (1992), pp. 25–48.
  - [52] R. RICO-MARTÍNEZ, R. ADOMAITIS, AND I. KEVREKIDIS, *Noninvertibility in neural networks*, *Computers & Chemical Engineering*, 24 (2000), pp. 2417–2433.
  - [53] S. SHVARTSMAN, C. THEODOROPOULOS, R. RICO-MARTÍNEZ, I. KEVREKIDIS, E. TITI, AND T. MOUNTZIARIS, *Order reduction for nonlinear dynamic models of distributed reacting systems*, *Journal of Process Control*, 10 (2000), pp. 177–184.
  - [54] S. SHVARTSMAN, C. THEODOROPOULOS, R. RICO-MARTÍNEZ, I. KEVREKIDIS, E. TITI, AND T. MOUNTZIARIS, *Order reduction for nonlinear dynamic models of distributed reacting systems*, *Journal of Process Control*, 10 (2000), pp. 177–184.
  - [55] S. Y. SHVARTSMAN AND I. G. KEVREKIDIS, *Nonlinear model reduction for control of distributed systems: A computer-assisted study*, *AIChE Journal*, 44 (1998), pp. 1579–1595.
  - [56] R. TEMAM, *Do inertial manifolds apply to turbulence?*, *Physica D: Nonlinear Phenomena*, 37 (1989), pp. 146–152.
  - [57] R. TEMAM, *Induced trajectories and approximate inertial manifolds*, *ESAIM: M2AN*, 23 (1989), pp. 541–561.
  - [58] T. TESHIMA, I. ISHIKAWA, K. TOJO, K. OONO, M. IKEDA, AND M. SUGIYAMA, *Coupling-based invertible neural networks are universal diffeomorphism approximators*, in *Proceedings of the 34th International Conference on Neural Information Processing Systems, NIPS’20*, Red Hook, NY, USA, 2020, Curran Associates Inc.
  - [59] E. S. TITI, *On approximate inertial manifolds to the navier-stokes equations*, *Journal of Mathematical Analysis and Applications*, 149 (1990), pp. 540–557.
  - [60] K. ZENG, C. E. P. D. JESÚS, A. J. FOX, AND M. D. GRAHAM, *Autoencoders for discovering manifold dimension and coordinates in data from complex dynamical systems*, 2023, <https://arxiv.org/abs/2305.01090>.
  - [61] K. ZENG, A. J. LINOT, AND M. D. GRAHAM, *Data-driven control of spatiotemporal chaos with reduced-order neural ode-based models and reinforcement learning*, *Proceedings of the Royal Society A: Mathematical, Physical and Engineering Sciences*, 478 (2022), p. 20220297.
  - [62] H. ZHANG, Y. LIU, AND R. MAULIK, *Semi-implicit neural ordinary differential equations for learning chaotic systems*, in *NeurIPS 2023 Workshop Heavy Tails in Machine Learning*, 2023.